THE ASTROPHYSICAL JOURNAL, 935:4 (19pp), 2022 August 10 https://doi.org/10.3847/1538-4357/ac7bde

Classification and Jet Power of Fermi Blazars

Lixia Zhang[1,2,3], Yi Liu[1,2,3], and Junhui Fan[1,2,3]
[1] Center for Astrophysics, Guangzhou University, Guangzhou 510006, People's Republic of China; fjh@gzhu.edu.cn
[2] Astronomy Science and Technology Research Laboratory of Department of Education of Guangdong Province, Guangzhou 510006, People's Republic of China
[3] Key Laboratory for Astronomical Observation and Technology of Guangzhou, Guangzhou 510006, People's Republic of China
Received 2021 November 9; revised 2022 April 29; accepted 2022 June 11; published 2022 August 8

Abstract

In this work, we compile a sample of 449 Fermi blazars with the luminosity of the broadline region, the black hole mass, the beam radio luminosity, and the jet power; obtain the beam power and the black hole spin; investigate the dividing line between BL Lacertae objects (BL Lacs) and flat-spectrum radio quasars (FSRQs) to identify the discrepancies in their dominant mechanisms; and revisit the dependence of the jet power on the disk accretion luminosity, the black hole mass, and the black hole spin. We come to the following conclusions. (1) A boundary of $\log(L_{\rm BLR}/L_{\rm Edd}) = -3.14$, separating the BL Lacs and the FSRQs, is obtained from the Bayesian analysis, which is consistent with the results from the literature. We employ the boundary to divide the blazar candidates of uncertain types into candidates for BL Lacs or FSRQs, and we find five changing-look blazars at the same time. (2) A strong correlation is found between black hole mass and intrinsic γ-ray luminosity, but a weaker correlation is found between black hole mass and observed γ-ray luminosity. The latter is weakened by jet effects: it is apparently weak for BL Lacs that have disordered amplification of the Doppler factor, since their mechanism is dominated by jets, while it is moderate for FSRQs, since their mechanism is dominated by accretion processes. (3) The jets of both FSRQs and BL Lacs are likely governed by the Blandford–Znajek mechanism.

Unified Astronomy Thesaurus concepts: Active galactic nuclei (16); Blazars (164); Jets (870); Black holes (162); Accretion (14)

Supporting material: machine-readable tables

1. Introduction

Blazars are the most powerful subclass of active galactic nuclei (AGNs), characterized by high luminosity, large and rapid variability, high and variable polarization, superluminal radio components, core-dominated nonthermal continua, bright γ-ray emission, etc. (Wills et al. 1992; Hartman et al. 1999; Abdo et al. 2010a, 2010b; Acero et al. 2015; Ackermann et al. 2015; Fan et al. 2016, 2017, 2018, 2021; Ajello et al. 2020). These extreme observational properties are caused by a beaming boosting effect, where the jet direction is close to the observer's line of sight (Blandford & Rees 1978; Urry & Padovani 1995). Blazars can be divided into flat-spectrum radio quasars (FSRQs), with strong emission lines, and BL Lacertae objects (BL Lacs), with weak or absent lines, on the basis of their emission-line behaviors. Namely, based on the equivalent widths (EWs) of the optical emission lines, blazars are classified as FSRQs with EW > 5 Å and as BL Lacs with EW < 5 Å (Stickel et al. 1991; Urry & Padovani 1995). In light of the ratio of the broadline region (BLR) luminosity to the Eddington luminosity, FSRQs and BL Lacs were separated with a dividing line of the order of $L_{\rm BLR}/L_{\rm Edd} \sim 5 \times 10^{-4}$, and the purpose of dividing by the Eddington luminosity here is to compare objects with different black hole masses (Ghisellini et al. 2011; Sbarrato et al. 2012).

According to theoretical models of jet formation, the jet originates from a spinning black hole, where the jet power is only related to the spin and mass of the black hole with the magnetic field at its horizon (Blandford & Znajek 1977, or to an accretion disk (Blandford & Payne 1982). Some studies show that the jet power of the Blandford–Znajek process derives from the black hole spin and the angular velocity of the magnetic field, which in turn depends on the type of accretion disk (Moderski & Sikora 1996; Ghosh & Abramowicz 1997). In the further understanding of the physics of and the central engines inside AGNs, the key point is to search for a relation between jets and accretion processes (Celotti et al. 1997; Cao & Jiang 1999). A correlation between jet power and accretion disk luminosity is expected if the squared magnetic field and the accretion rate are proportional (Ghisellini et al. 2014), and it is reported that the magnetic field is correlated with the accretion disk luminosity for radio-loud active galaxies (Zamaninasab et al. 2014). There are many works exploring such an indirect correlation between jet power and accretion disk luminosity through the correlation between γ-ray/radio luminosity and BLR luminosity, and a strong correlation is obtained (Celotti et al. 1997; Cao & Jiang 1999; Sbarrato et al. 2012; Ghisellini et al. 2014; Xiong & Zhang 2014; Zhang et al. 2020). Meier (2002) has proposed that the spin and mass of the central black hole also contribute to the jet power, besides the contribution from accretion processes, which means that the jet power is larger than the accretion disk luminosity.

In the physical structure of an AGN, Urry & Padovani (1995) have illustrated that the basic source of the AGN's luminosity is the gravitational potential energy from a supermassive black hole at the AGN's center. For an astrophysical black hole, the black hole mass and the black hole spin are two defining properties that can be measured. Although it is difficult to estimate the central black hole masses accurately, some methods for assessing the black hole masses have been proposed: the reverberation mapping technique (Wandel et al. 1999; Kaspi et al. 2000; Li et al. 2021; Feng et al. 2021a, 2021b); the gas and stellar dynamics technique

(Genzel et al. 1997; Magorrian et al. 1998); the variability timescale technique (Cheng et al. 1999; Fan et al. 1999; Fan 2005); the broadline width technique (Laor 1998; McLure & Dunlop 2001); empirical relation techniques, such as the M_{BH}–σ relation (Merritt & Ferrarese 2001; Wu et al. 2002); virial estimator techniques, including broad H α, H β, Mg II, and C IV estimators from emission lines (McLure & Dunlop 2004; Vestergaard & Peterson 2006; Vestergaard & Osmer 2009; Shen et al. 2011; Shaw et al. 2012); and so on.

There has been great progress in the measurement of black hole masses, but it is more challenging to study the black hole spin directly, with only a few observations: rapidly rotating black holes have been suggested from observations of Seyfert galaxies and observations in X-ray of active galaxies (Wilms et al. 2001; Fabian et al. 2002; Crummy et al. 2006), and a large black hole spin has been suggested from observations of the Galactic center black hole (Genzel et al. 2003; Aschenbach et al. 2004). Daly (2009a) presented a method independent of a model to estimate the black hole spin, using the outflow energy and black hole mass. Theoretical prediction models that have been made for black hole spin include the Blandford–Znajek model (Blandford & Znajek 1977) and the Meier model (Meier 1999), while the hybrid Meier model includes the characteristics of the Blandford–Znajek model and the Blandford–Payne model. In the context of the models combined with the Blandford–Znajek model, and the Meier model, which is in the form of a similar function, the black hole spin can be studied from the black hole mass and the beam power (the energy that is carried by the outflow per time) of the radio sources, based on the hypothesis that the black hole spin energy can power the AGN outflows (Daly 2009b). Daly (2016) studied the relationship between beam power, accretion disk bolometric luminosity, and Eddington luminosity, to estimate the spin function with general equations for beam power and accretion disk bolometric luminosity. Daly (2019) then estimated the black hole spin, following and extending the method from Daly (2016).

However, there are some issues that still remain open. In a recent study, Chen et al. (2021) used a multiple regression to link the jet power with the accretion luminosity, black hole mass, and black hole spin, which may shed some light on the way in which the jet power depends on those parameters in Fermi blazars, and whether the jet formation is governed by the Blandford–Znajek process or the Blandford–Payne process. Another problem is to figure out the distinctions between the dominant mechanisms of FSRQs and BL Lacs, respectively, and to compare the relationships between jet power and accretion luminosity/black hole mass/black hole spin for the two subclasses. Moreover, an FSRQ with a strong line emission may appear as a BL Lac, and, vice versa, a BL Lac with EW > 5 Å may be identified as an FSRQ (Sbarrato et al. 2012), while the objects lacking optical spectra that are marked as blazar candidates of uncertain types (BCUs; Ackermann et al. 2015; Acero et al. 2015), should be divided into either BL Lac or FSRQ candidates, otherwise these BCUs will introduce some confusion into these classification schemes. It is worth noticing that the samples studied in other works (Ghisellini et al. 2011; Sbarrato et al. 2012) are too limited to be conclusive regarding the dividing line for classification using $L_{\mathrm{BLR}}/L_{\mathrm{Edd}}$. This work is mainly aimed at setting a boundary between FSRQs and BL Lacs with $L_{\mathrm{BLR}}/L_{\mathrm{Edd}}$, investigating the correlations among jet power, accretion luminosity, black hole mass, and black hole spin, and exploring the jet formation mechanism in a larger sample. It is arranged as follows. Section 2 gives the sample, Section 3 gives the methods and results, and Sections 4 and 5 present the discussions and conclusions. The cosmology constant is adopted by a Λ cold dark matter (CDM) model, with $H_0 = 71$ km s^{-1} Mpc^{-1}, $\Omega_\Lambda = 0.73$, and $\Omega_M = 0.27$ throughout this paper (Komatsu et al. 2011).

2. Sample

For the purpose of studying the boundary and the jet formation mechanism, we try to obtain a large sample of Fermi blazars with available BLR luminosity, γ-ray luminosity, black hole mass, beam radio luminosity, and jet power. To do this, we collected the BLR luminosity from the available references, then matched those selected blazars with the released Fermi Large Area Telescope (LAT) catalogs: the LAT 1 yr Source Catalog (1FGL); the LAT 2 yr Source Catalog (2FGL); the LAT 4 yr Source Catalog (3FGL); the LAT 8 yr Source Catalog (4FGL); and the LAT 10 yr Source Catalog (4FGL-DR2). First, the selected blazar with available BLR data was cross-matched with 4FGL-DR2 (Ballet et al. 2020), then we could calculate its γ-ray luminosities from 4FGL-DR2 (containing 4FGL), and if the selected blazar with available BLR data did not match with 4FGL-DR2, then we would conduct cross checks with 3FGL, 2FGL, or 1FGL, and the γ-ray photon index and integral flux in the corresponding Fermi FGL catalogs would obtained to calculate its γ-ray luminosity.

The BLR luminosities were collected from the following works: Celotti et al. (1997), Cao & Jiang (1999), Liu et al. (2006), Shen et al. (2011), Chai et al. (2012), Sbarrato et al. (2012), Shaw et al. (2012), Ghisellini et al. (2014), Xiong & Zhang (2014), Zhang et al. (2020), Chen et al. (2021), and references therein.

The black hole masses in this work are found in the available literature and the present work. The literature includes Celotti et al. (1997), Cao & Jiang (1999), Liu et al. (2006), Shen et al. (2011), Chai et al. (2012), Sbarrato et al. (2012), Shaw et al. (2012), Ghisellini et al. (2014), Xiong & Zhang (2014), and references therein. The black hole masses obtained for 50 sources from Zhang et al. (2020) are also calculated in this work. In this case, we can see that the black hole masses for the whole sample consist of three components. First, there are 379 blazars whose black hole masses are related to the continuum and BLR emissions: of these 379 sources, the data for 307 blazars were collected from various references, where the available black hole masses were estimated by continuum emissions, and for the other 72 blazars, their black hole masses were calculated using the BLR emissions in this work, including 50 blazars with new BLR luminosities and FWHMs from the fitted broad emission spectrum from Zhang et al. (2020), and 22 blazars with available BLR luminosities but FWHMs that needed to be hunted down from references. Second, there are 48 blazars whose black hole masses are calculated from other empirical formulae: here, we use $M - M_i$, $M - t$, and $M - \sigma$ to indicate the black hole masses, which are derived from the magnitude, the timescale, and the stellar velocity dispersion. Finally, there are 22 blazars without available black hole masses calculated from any of the above methods. It was found that eight of these 22 blazars were given average values in the work of Sbarrato et al. (2012), while for the other 14 blazars we adopted the average mass values from the corresponding subclasses (BL Lacs, FSRQs, or BCUs in this work) as their black hole masses.

Intema et al. (2017) presented the 150 MHz flux density for a large number of sources detected by the Giant Metrewave Radio Telescope (GMRT), and the available radio flux density at 150 MHz can be taken as the flux density at 151 MHz (F_{151}). In this sense, there are 415 common blazars with a beam radio flux density detected by GMRT in this work. Based on the 150 MHz data, the beam power (L_j) and the black hole spin (j) can be calculated. The jet power is collected from Chen (2018). In total, we obtained 449 Fermi blazars with both BLR luminosity and γ-ray luminosity, 439 Fermi blazars coming from 4FGL-DR2, five Fermi blazars coming from 3FGL, and five Fermi blazars coming from 1FGL. Of our whole sample of 449 blazars, there are 112 BL Lacs, 308 FSRQs, and 29 BCUs. The sample is listed in Table 1.

3. Methods and Results

3.1. Calculation for Luminosity

The calculation of the total BLR luminosity was described in Celotti et al. (1997), based on the model of Gaskell et al. (1981) and Francis et al. (1991). Following the work by Celotti et al. (1997), and given the sum of the observed luminosities in a certain number of broad lines $\sum_i L_{i,\rm obs}$, one can obtain the total $L_{\rm BLR}$ by:

$$L_{\rm BLR} = \sum\nolimits_i L_{i,\rm obs}\frac{\langle L^{\star}_{\rm BLR}\rangle}{\sum_i L^{\star}_{i,\rm est}}, \tag{1}$$

where $\sum_i L^{\star}_{i,\rm est}$ is the sum of the luminosities from the same lines, estimated through the adopted line ratios. Here, $L^{\star}_{{\rm Ly}\ \alpha}$ is normalized to 100, $L^{\star}_{\rm H\alpha}$, $L^{\star}_{\rm H\beta}$, $L^{\star}_{\rm Mg\ \ II}$, and $L^{\star}_{\rm C\ \ IV}$ are set as 77, 22, 34, and 63, respectively, and $L^{\star}_{\rm BLR}$ is set as 555.6, so the line ratio is theoretically essentially constant for different objects. If there is only one line, $H\ \alpha$, for example, the observed luminosity is $L_{\rm H\alpha}$, and it corresponds to a ratio of $L^{\star}_{\rm H\alpha}/L^{\star}_{\rm BLR} = 77/555.6$, meaning that its BLR luminosity can be estimated by dividing the measured line luminosity by its line ratio: $L_{\rm BLR} = L_{\rm H\alpha}\frac{\langle L^{\star}_{\rm BLR}\rangle}{L^{\star}_{\rm H\alpha}}$.

When more than one line is present, to combine the different BLR luminosities derived from the individual lines, we calculate the total $L_{\rm BLR}$ by weighting it from their measured line luminosities:

$$L_{\rm BLR} = \sum\nolimits_i L_{i,\rm obs}\frac{\langle L^{\star}_{\rm BLR}\rangle}{L^{\star}_{i,\rm est}}\frac{L_{i,\rm obs}}{\sum_i L_{i,\rm obs}}. \tag{2}$$

For instance, if there are H β and MgII lines for one source, we will calculate the total $L_{\rm BLR}$ by weighting $L_{\rm H\beta}$ and $L_{\rm MgII}$:

$$L_{\rm BLR} = L_{\rm H\beta}\frac{\langle L^{\star}_{\rm BLR}\rangle}{L^{\star}_{\rm H\beta}}\frac{L_{\rm H\beta}}{L_{\rm H\beta}+L_{\rm MgII}} + L_{\rm MgII}\frac{\langle L^{\star}_{\rm BLR}\rangle}{L^{\star}_{\rm MgII}}\frac{L_{\rm MgII}}{L_{\rm H\beta}+L_{\rm MgII}}.$$

The γ-ray luminosity is calculated as $L_{\gamma} = 4\pi\ d_L^2\ (1+z)_{\alpha_{\gamma}\ -1}F_{\gamma}$, where z is redshift; d_L is a luminosity distance calculated from the ΛCDM model (Capelo & Natarajan 2007): $d_L = (1+z)\cdot\frac{\rm c}{\rm H_0}\cdot\int_1^{1+z}\frac{1}{\sqrt{\Omega_{\rm M}x^3\ +\ 1-\Omega_{\rm M}}}dx$; $(1+z)_{\alpha_{\gamma}-1}$ is a K-correction with spectral index α_{γ} ($f_{\nu}\propto\nu_{-\alpha_{\gamma}}$) at frequency ν, here $\alpha_{\gamma} = \alpha_{\rm ph} - 1$; and $\alpha_{\rm ph}$ and F_{γ} are the photon index and the integral flux in the γ-ray band from the Fermi FGL catalogs, respectively. For the details of the computational process, see Fan et al. (2012).

The beam radio luminosity at 151 MHz was calculated as $L_{\rm R} = 4\pi\ d_L^2\ (1+z)^{\alpha}_{\rm R\ -1}F_{151}$, where $\alpha_{\rm R}$ is the radio spectral index, adopted with the critical value of $\alpha_{\rm R} = 0.8$ for 151 MHz flux density from Cassaro et al. (1999). We can now conduct statistical analyses for the whole sample, obtaining the following results: the logarithm of the BLR luminosity is in a range of 41.28–47.07 (erg s^{-1}), with a mean value of 44.32 ± 1.06 (erg s^{-1}); the logarithm of the γ-ray luminosity is in a range of 42.82–48.61 (erg s^{-1}), with a mean value of 46.15 ± 1.10 (erg s^{-1}); and the logarithm of the beam radio luminosity at 151 MHz is in a range of 38.07–44.42 (erg s^{-1}), with a mean value of 42.19 ± 1.18 (erg s^{-1}).

3.2. Black Hole Masses

The reverberation mapping can measure the size and kinematics of the BLR from the time lags of the emission lines in response to the continuum light curves (Kaspi et al. 2000), and it is a promising technique for estimating the black hole masses for AGNs. Assuming that the gravity of the central supermassive black hole is responsible for the dominant mechanism of the BLR dynamics, then the virial black hole mass can be estimated as:

$$M_{\rm BH} = \frac{R_{\rm BLR}V^2_{\rm BLR}}{G}, \tag{3}$$

where $R_{\rm BLR}$ is the BLR size that can be obtained from the time delay of the emission lines to the continuum, $V_{\rm BLR}$ is the velocity of the gas of the BLR, and G is the gravitational constant (McLure & Dunlop 2004; Liu et al. 2006; VP06). However, the reverberation mapping technique needs long-term monitoring of both the continuum and the emission lines (Oshlack et al. 2002), and this is difficult to achieve for all the Fermi blazars. If the continuum luminosity (λL_{λ}) is intended as the size of the BLR, and the broadline width FWHM is intended as the velocity of the BLR, then the virial black hole masses are estimated from a relation in the following form:

$$\log\left(\frac{M_{\rm BH}}{M_{\odot}}\right) = a_* + b_*\log\left(\frac{\lambda L_{\lambda}}{10^{44}{\rm erg\ s^{-1}}}\right) + 2\log\left(\frac{\rm FWHM}{\rm km\ s^{-1}}\right), \tag{4}$$

where the coefficients a_* and b_* are empirically calibrated among different broad emission lines; McLure & Dunlop (2004; hereafter, MD04) give the values of a_* and b_* for H β and Mg II, while Vestergaard & Peterson (2006; hereafter, VP06) give the values for C IV. Shen et al. (2011; hereafter, S11) fitted the continuum luminosity to the Mg II and C IV luminosities, and Shaw et al. (2012; hereafter, S12) fitted the continuum luminosity to the H β luminosity. S11 presented the virial black hole mass based on the broadline luminosity and FWHM for H α, following Greene & Ho (2005), which is shown in Equation (5). Likewise, we summarized the virial black hole mass, combining the calibration parameters of a_* and b_* with the correlations of λL_{λ} versus $L_{\rm BLR}$, then obtained the virial black hole masses for the H β line from MD04 and S12, for the Mg II line from MD04 and S11, and for the

Table 1
Sample of Blazars

Name (1)	Class (2)	z (3)	log $L_{\rm BLR}$ (4)	line (5)	ref (6) (7)	log M (8)	line (9)	ref (10)	log L_γ (11)	log $L_{\rm R}$ (12)	log L_j (13)	j (14)	log $P_{\rm jet}$
4FGL J0004.4-4737	CF	0.880	44.11	Mg II	S12	7.85	Mg II	S12	46.01	42.45	43.90	0.76	46.20
4FGL J0006.3-0620	CB	0.347	43.14	H α	S89	8.53	mean-TW		44.56	41.87	43.40	0.51	
4FGL J0008.4+1455	CBU	0.045	42.32	H β	S12	8.19	H β	S12	43.02	38.43	40.45	0.04	
4FGL J0011.4+0057	CF	1.493	44.63	Mg II, C IV	S12	8.8, 8.09	Mg II, C IV	S12	46.62	42.12	43.62	0.34	
4FGL J0014.1+1910	CB	0.477	42.70		G14	8.30		C21	45.06	40.54	42.27	0.21	
4FGL J0016.2-0016	CF	0.226	44.91	Mg II, C IV	S11	8.55,9.04	Mg II, C IV	S11	46.46	43.11	44.47	0.58	46.40
4FGL J0016.5+1702	CF	1.709	45.28	Mg II, C IV	S12	9.36, 9.15	Mg II, C IV	S12	46.34	41.95	43.47	0.13	
4FGL J0017.5-0514	CF	0.227	43.79	H β	S12	7.55	H β	S12	44.72	40.65	42.36	0.22	45.10
4FGL J0019.6+7327	CF	1.781	44.99	$L_{{\rm y}\ \alpha}$, C IV, Mg II	L96	8.93		Z09	47.26	43.10	44.46	0.52	
4FGL J0022.0+0006	CB	0.306	42.56	H α, H β	Sb12	8.49	M - σ	P11	44.62	40.77	42.46	0.26	
4FGL J0023.7+4457	CF	2.023	44.28	C IV	S12	7.78	C IV	S12	46.39	42.14	43.63	0.58	46.50
4FGL J0024.7+0349	CF	0.545	43.80	Mg II	S12	7.76	Mg II	S12	45.03	40.66	42.37	0.19	45.60
4FGL J0042.2+2319	CF	1.426	44.63	Mg II	S12	9.01	Mg II	S12	46.54	42.70	44.12	0.41	46.70
4FGL J0043.8+3425	CF	0.966	44.02	Mg II	S12	8.01	Mg II	S12	46.99	41.61	43.18	0.36	45.80
4FGL J0044.2-8424	CF	1.032	44.88	Mg II	S12	8.68	Mg II	S12	45.85				46.30
......	......	......	......	......	......	......	......	......	......	......	......	......	......
......	......	......	......	......	......	......	......	......	......	......	......	......	......

Notes. Column (1): name—the superscripts of "1" and "3" denote the 1FGL blazars and the 3FGL blazars, respectively; otherwise, they are 4FGL blazars from 4FGL-DR2. Column (2): classification—"CF" and "CB" are the blazars confirmed as FSRQs and BL Lacs, respectively; "CFU" and "CBU" are the BCUs classified as FSRQs and BL Lacs resulting from the classification in Section 3.2; "CB-CF" is a BL Lac classified as an FSRQ by the 1D and 2D methods; "CF-CB" is an FSRQ classified as a BL Lac by both the 1D and 2D methods; "CB-CF/CB" is a BL Lac classified as an FSRQ by the 1D method but classified as a BL Lac by the 2D method; "CB-CF-CL" is a changing-look blazar responsible for a case of "CB-CF"; and "UF" is a BCU that was previously classified as an FSRQ candidate. Column (3): redshift (z). Column (4): logarithm of the BLR luminosity in units of erg $\rm s^{-1}$ (log $L_{\rm BLR}$). Column (5): the estimators for Column (4), including lines of H α, H β, Mg II, C IV, H γ, and $L_{{\rm y}\ \alpha}$. Column (6): the references for Column (4). Column (7): logarithm of the black hole mass log M in units of solar mass (log $(M_{\rm BH}/M_\odot)$); the superscript of "e" denotes the estimated black hole masses for 22 blazars (of the 72 blazars that we calculated) with FWHMs searched from references. Column (8): the estimators for Column (7), including lines of H α, H β, Mg II, and C IV; "$M - M_{\rm i}$," "$M - t$," and "$M - \sigma$" denote the black hole masses calculated by the magnitude (optical-B or optical-R band), timescale, and dispersion of the velocity, respectively, from the empirical formulae; "mean-Sb12" denotes the black hole masses that were obtained by the mean value from Sbarrato et al. (2012); and "mean-TW" denotes the black hole masses that were obtained by the mean value from each subclass in this work. Column (9): the references for Column (7). Column (10): logarithm of the γ-ray luminosity (1 ∼100 GeV) in units of erg $\rm s^{-1}$ (log L_γ). Column (11): logarithm of the radio luminosity at 151 MHz in units of erg $\rm s^{-1}$ (log $L_{\rm R}$). Column (12): logarithm of the beam power at 151 MHz in units of erg $\rm s^{-1}$ (log L_j). Column (13): the spin of the black hole (j). Column (14): logarithm of the jet power SED compiled from Chen (2018) in units of erg $\rm s^{-1}$ (log $P_{\rm jet}$). B81: Baldwin et al. (1981); B89: Baldwin et al. (1989); B94: Brotherton et al. (1994); B96: Brotherton (1996); B99: Baker et al. (1999); B03: Barth et al. (2003); BM87: Browne & Murphy (1987); C92: Corbin (1992); C97: Celotti et al. (1997); C03: Cao (2003); C12: Chai et al. (2012); C18: Chen (2018); C21: Chen et al. (2021); d94: di Serego Alighieri et al. (1994); E89: Espey et al. (1989); F83: Fricke et al. (1983); F04: Fan & Cao (2004); G01: Gu et al. (2001); G14: Ghisellini et al. (2014); GW94: Gelderman & Whittle (1994); H78: Hunstead et al. (1978); J84: Junkkarinen (1984); J91: Jackson & Browne (1991); K85: Kinney et al. (1985); L96: Lawrence et al. (1996); L03: Liang & Liu (2003); M92: Morganti et al. (1992); M96: Marziani et al. (1996); M99: McIntosh et al. (1999); N79: Neugebauer et al. (1979); O84: Oke et al. (1984); O94: Osmer et al. (1994); O02: Oshlack et al. (2002); P89: Perez et al. (1989); P04: Peterson et al. (2004); P05: Pian et al. (2005); P06: Panessa et al. (2006); P11: Plotkin et al. (2011); R84: Rudy (1984); RS80: Richstone & Schmidt (1980); S81: Smith et al. (1981); S93a: Stickel et al. (1993a); S93b: Stickel et al. (1993b); S89: Stickel et al. (1989); S11: Shen et al. (2011); Sb12: Sbarrato et al. (2012); SC95: Scarpa et al. (1995); S12: Shaw et al. (2012); SJ85: Sitko & Junkkarinen (1985); SK93a: Stickel & Kuehr (1993); SK93b: Stickel & Kuhr (1993); SS91: Steidel & Sargent (1991); T93: Tadhunter et al. (1993); TW: black hole mass calculated in this work; W84: Wampler et al. (1984); W86: Wilkes (1986); W95: Wills et al. (1995); W02: Woo & Urry (2002); W04: Wang et al. (2004); W05: Woo et al. (2005); WM96: Warren & Møller (1996); X91: Xie et al. (1991); X04: Xie et al. (2004); Z09: Zhou & Cao (2009); Z20: Zhang et al. (2020). This table is available in its entirety in machine-readable form.

(This table is available in its entirety in machine-readable form.)

C IV line from VP06 and S11, which are expressed in Equations (6)–(8):

$$\log\left(\frac{M_{\rm BH}}{M_\odot}\right)_{\rm H\alpha} = 0.379 + 0.43 \log \times \left(\frac{L_{\rm H\alpha}}{10^{42}{\rm erg\ s^{-1}}}\right) + 2.1 \log\left(\frac{{\rm FWHM}_{H\alpha}}{\rm km\ s^{-1}}\right), \quad (5)$$

$$\log\left(\frac{M_{\rm BH}}{M_\odot}\right)_{\rm H\beta} = (1.63 \pm 0.04) + (0.49 \pm 0.03) \times \log\left(\frac{L_{\rm H\beta}}{10^{44}{\rm erg\ s^{-1}}}\right) + 2 \log\left(\frac{{\rm FWHM}_{H\beta}}{\rm km\ s^{-1}}\right), \quad (6)$$

$$\log\left(\frac{M_{\rm BH}}{M_\odot}\right)_{\rm Mg\,II} = (1.70 \pm 0.07) + (0.63 \pm 0.00) \times \log \times \left(\frac{L_{\rm Mg\,II}}{10^{44}{\rm erg\ s^{-1}}}\right) + 2 \log\left(\frac{{\rm FWHM}_{\rm Mg\,II}}{\rm km\ s^{-1}}\right), \quad (7)$$

$$\log\left(\frac{M_{\rm BH}}{M_\odot}\right)_{\rm C\,IV} = (1.52 \pm 0.22) + (0.46 \pm 0.01) \times \log \times \left(\frac{L_{\rm C\,IV}}{10^{44}{\rm erg\ s^{-1}}}\right) + 2 \log\left(\frac{{\rm FWHM}_{\rm C\,IV}}{\rm km\ s^{-1}}\right). \quad (8)$$

Therefore, one can use the luminosities and FWHMs of the H α, H β, Mg II, or C IV lines to estimate the black hole masses. In this work, there are 72 blazars with luminosities and FWHMs for broad emission lines, but they have no available central black hole masses. Of them, the FWHM data are available for 50 sources in Zhang et al. (2020; 43 sources have available FWHMs for the Mg II line, three sources have FWHMs only for the Hα line, and four sources have FWHMs only for the C IV line), and the FWHM data for the other 22 sources are found from earlier original references (13 sources have FWHMs for the Mg II line, one source has an FWHM only for the Hα line, and eight sources have FWHMs only for the C IV line). Based on the BLR luminosity and FWHM data for those 72 blazars, we estimated the black hole masses from the Hα line for four blazars, from the Mg II line for 56 blazars, and from the C IV line for 12 blazars.

For the other 22 blazars without black hole masses or available FWHM data in the literature, eight sources were given averaged values for their black hole masses from Sbarrato et al. (2012), while the remaining 14 sources (six FSRQs, five BL Lacs, and three BCUs) are without available FWHM data from the literature. So far, we have obtained black hole masses for 435 blazars, which give averaged values log $(M_{\rm BH}/M_\odot) = 8.49$ for 302 FSRQs, log $(M_{\rm BH}/M_\odot) = 8.53$ for 107 BL Lacs, and log $(M_{\rm BH}/M_\odot) = 8.46$ for 26 BCUs. We have adopted the averaged black hole mass values for the subclasses of blazars as the black hole masses for the remaining 14 sources, namely, log $(M_{\rm BH}/M_\odot) = 8.49$ are adopted for six FSRQs, log $(M_{\rm BH}/M_\odot) = 8.53$ for five BL Lacs, and log $(M_{\rm BH}/M_\odot) = 8.46$ for three BCUs. As a brief summary, these 22 sources are given with averaged black hole masses, eight of them are from Sbarrato et al. (2012) and 14 are from this work. In total, we obtain the black hole mass log $(M_{\rm BH}/M_\odot)$, which is in a range of 6.35–10.21, with a mean value of 8.50 ± 0.54, for the whole sample.

3.3. Ratio of BLR Luminosity to Eddington Luminosity

The Eddington luminosity is expressed as

$$L_{\rm Edd} = 1.3 \times 10^{38}\left(\frac{M_{\rm BH}}{M_\odot}\right) {\rm erg\ s^{-1}}. \quad (9)$$

The BLR luminosity is compared to the corresponding Eddington luminosity, and the ratio $\log(L_{\rm BLR}/L_{\rm Edd})$ is defined as the parameter $l_{\rm BLR}$. The histogram of $l_{\rm BLR}$ is plotted in Figure 1, and one can clearly see the signs of multiple components. To classify the FSRQs and BL Lacs by the parameter $l_{\rm BLR}$, the Gaussian Mixture Modeling (GMM) clustering method is performed on the distribution of $l_{\rm BLR}$. The idea of GMM clustering is to assume that the parameter obeys a distribution that is a mixture of several Gaussian distributions, whose parameters are unknown. First, given a set of parameters, a Gaussian mixture probability can be obtained; then, given the $l_{\rm BLR}$ observed, a corresponding probability can be given; and the probability of all $l_{\rm BLR}$ observed is equal to the product of the probabilities corresponding to each $l_{\rm BLR}$ observed. The actual sample obtained from the $l_{\rm BLR}$ observed should correspond to the case where this probability is the maximum, called the maximum-likelihood probability. By finding the set of Gaussian distributions corresponding to the maximum-likelihood probability, their mixed probabilities can be used as a good approximation of the probabilities obeyed by the sample. We use the R package "Mclust" (Fraley & Raftery 2002; Fraley et al. 2012; Scrucca et al. 2016) to perform the GMM clustering. Bayesian Information Criteria (BIC), with different types and numbers of models, were obtained and are drawn in Figure 2. Two types of model are used in the calculation of the BIC: one is the V (unequal variance) model and the other is the E (equal variance) model. For the case consisting of certain components, the BIC reaches the maximum. For the $l_{\rm BLR}$ of a given source, its probability of belonging to a certain Gaussian component is given by the GMM, and the probability densities of each Gaussian component are plotted in Figure 1. The $l_{\rm BLR}$ at the intersection of the two density curves has an equal probability of belonging to one of these two components, and thus can be used as the boundary for classification.

In Figure 1(a), there are three components in the case of the *V* model, according to the BIC values from Figure 2, where the two components expressed in red curves have similar mean values: the broad one has a mean value of -1.93 ± 0.72, while the narrow one has a mean value of -1.87 ± 0.25. These two components should actually be the same component, because they are unable to be separated. In this case, we set two components in the case of the *V* model; see Figure 1(b). In Figures 1(b) and 1(c), the FSRQs have a larger GMM membership probability, while the BL Lacs have a smaller GMM membership probability: the right component of the intersection is for FSRQs, since they have strong BLR emissions, while the left component of the intersection is for BL Lacs, due to their featureless BLR emissions. For the main purpose of the GMM, the *V* option is essential, but a considerable proportion of the left component in Figure 1(b) with the *V* model overwhelms the intersection with the larger dispersion, implying that these BL Lacs have strong BLR

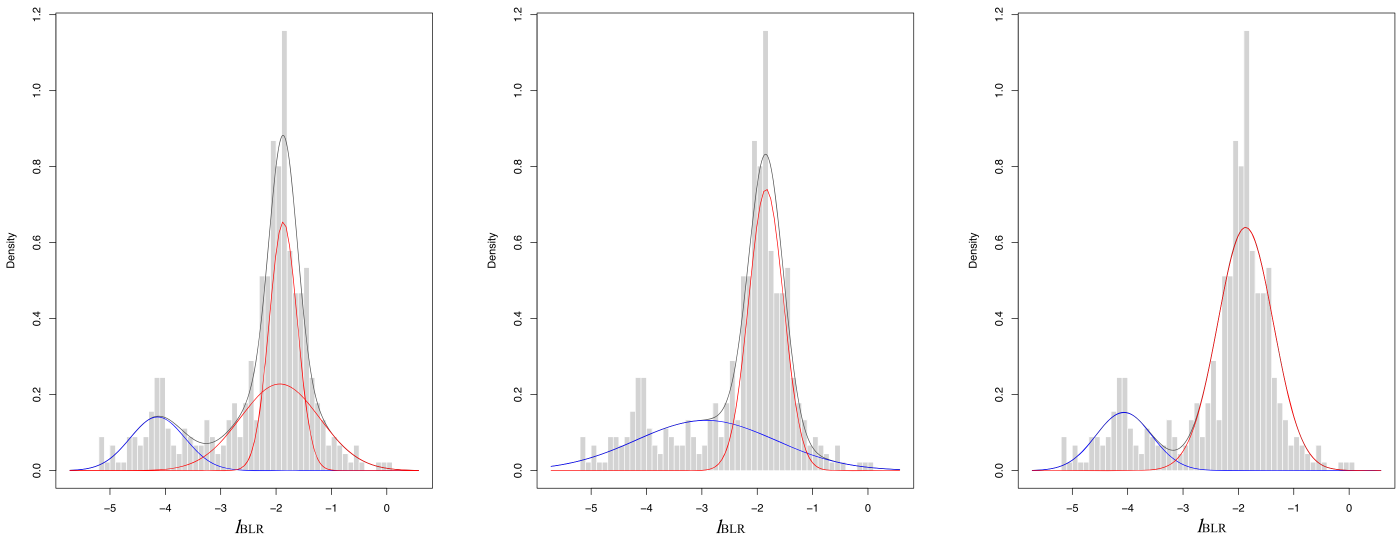

Figure 1. The distributions and densities for the 1D data of $l_{\rm BLR} = \log(L_{\rm BLR}/L_{\rm Edd})$, with bins of 0.1. The left panel shows three components from the *V* model. The medium panel shows two components from the *V* model. The right panel shows two components from the *E* model. The black curves represent the density distribution of the whole sample, the blue curves represent those of the left component, divided as the BL Lac population, and the red curves represent those of the right component, divided as the FSRQ population.

emissions, which is physically contradictory. In Figure 1(c), with the *E* model, the left component is less than the right component, except for only a few blazars, while the classification with the *E* model in Figure 1(c) accords with the physical characteristics of BL Lacs and FSRQs. For a brief summary, the mean values and standard deviations of the two subclasses, with more information for model *V* and model *E*, are listed in Table 2.

Therefore, the *E* model in Figure 1(c) is taken as the criterion for our work, and the *E* model presents an intersection at −3.14 for $l_{\rm BLR}$. Choosing the $l_{\rm BLR}$ value at the intersection as the boundary for all the sources, the classifications can then be set: $l_{\rm BLR} < -3.14$ for BL Lacs and $l_{\rm BLR} > -3.14$ for FSRQs. Therefore, we can use this classification to classify a BCU located in the region of FSRQs as a CFU (regarded as an FSRQ candidate), and a BCU located in the region of BL Lacs as a CBU (regarded as a BL Lac candidate). Based on this dividing criterion for 1D data (the 1D method, for short), the results show that 21 BCUs are CFUs and eight BCUs are CBUs.

We also employ a 2D scattering diagram of BLR luminosity and Eddington luminosity for our whole sample (the 2D method, for short). We mark them with different colors and symbols, as shown in Figure 3, and we can identify the upper cluster as belonging to FSRQs, due to their strong broadline emissions, and the lower cluster as belonging to BL Lacs, due to their weak broadline emissions. Accordingly, it is relevant to point out each classification from the various approaches: the result derived from the 1D method with $l_{\rm BLR} = -3.14$ is shown as a solid line, while the one derived from Ghisellini et al. (2011; hereafter, G11) with $l_{\rm BLR} = -3.30$ is shown as a dotted line (from $L_{\rm BLR}/L_{\rm Edd} \sim 5 \times 10^{-4}$). These two dividing lines are shown in Figure 4.

3.4. Jet Power

Ghisellini et al. (2014) expressed the jet power with diverse sources as

$$P_{\rm jet} = 2\pi R_{\rm em}^2 c\Gamma^2 (U_{\rm B} + U_{\rm e} + U_{\rm p} + U_{\rm rad}), \quad (10)$$

where the factor of 2 represents two jets, $R_{\rm em}$ is the radius of the emitting region, Γ is the bulk Lorentz factor, and $U_{\rm B}$, $U_{\rm e}$, $U_{\rm p}$, and $U_{\rm rad}$ are the comoving energy density of the magnetic field, that of the relativistic electrons, that of the protons, and that of the produced radiation, respectively. The density of the jet can be obtained from simulations of the observed spectral energy distribution (SED), then used to calculate the energy carried by the jet. Recently, Chen (2018) calculated the jet power based on broadband SEDs for 1392 γ-ray-loud AGNs (Fan et al. 2016), providing good reference values for the jet power of Fermi blazars. In his work, he assumed that the jet power is made by electrons and protons, and the timescale is set as one day. From his work, we found 355 common sources with our sample, and we found the jet power to be in a range of 44.10–48.40 (erg $\rm s^{-1}$), with a mean value of 46.27 ± 0.72 (erg $\rm s^{-1}$) for the 355 sources.

3.5. Beam Power

The kinetic jet power is obtained from the lobe energy content divided by the corresponding age of the radio galaxies (Rawlings & Saunders 1991). Later, Willott et al. (1999) proposed a relation of kinetic jet power with extended radio luminosity at 151 MHz,

$$P_{\rm jet}^{\rm radio} \simeq 3 \times 10^{38} \zeta^{3/2} L_{\rm ext,151}^{6/7} \,{\rm W}, \quad (11)$$

where ζ, an unknown variety, is in a range of $1 \leqslant \zeta \leqslant 20$, and can be calculated using the minimum energy density of the radio lobe (Miley 1980), based on the jet model (Falle 1991), and $L_{\rm ext,\ 151}$ is the extended radio luminosity at 151 MHz, in units of 10^{28} W $\rm Hz^{-1}$ $\rm sr^{-1}$, where the extended radio luminosity at low frequency emerges in Equation (11), due to a routine: the X-ray cavities inflated by the AGN jet (Allen et al. 2006) can estimate the "work" done to expand the cavities, and the kinetic power is estimated by dividing this "work" by the cavity ages and is independent of the assumption of minimal energy (Bîrzan et al. 2008; Cavagnolo et al. 2010; Meyer et al. 2011).

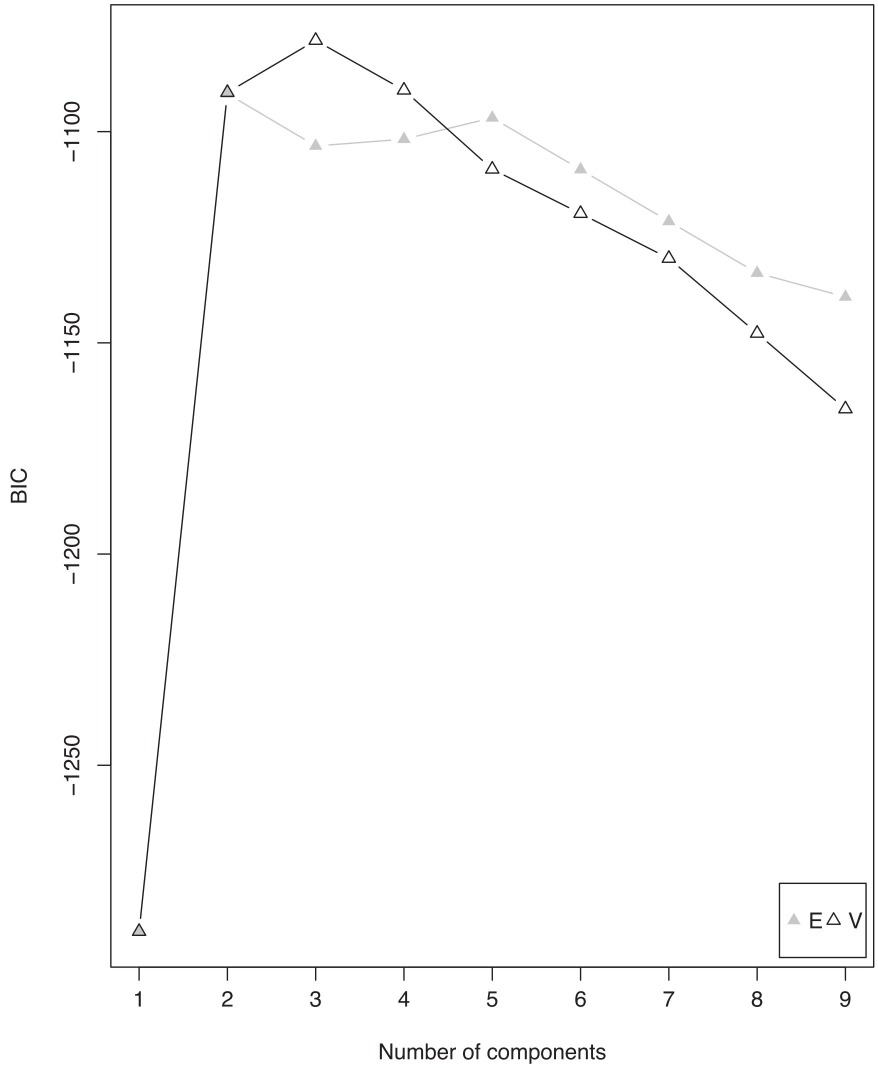

Figure 2. BIC values for models with up to nine clusters applied to the density distribution of $l_{\rm BLR} = \log(L_{\rm BLR}/L_{\rm Edd})$. The hollow triangles stand for the V (unequal variance) model, while the solid triangles stand for the E (equal variance) model.

The parent population of the BL Lacs comprises Fanaroff and Riley type I (FR I) radio galaxies (Fanaroff & Riley 1974) with low luminosity, and the parent population of the FSRQs comprises FR II radio galaxies with high luminosity (Padovani 1992). Equation (11) can be applied to both FR II radio galaxies and radio quasars, and Cao (2003) used it to estimate the jet power as an approximation for BL Lacs whose radio properties are similar to those of radio quasars, with a lower limit of $\zeta = 1$, as the beam power can provide information to determine the black hole spin (O'Dea et al. 2009; Daly 2011). Therefore, we can adopt the following relation (derived from Equation (11), with $\mathrm{sr} = 4\ \pi$) to calculate the beam power for both BL Lacs and FSRQs (Chen et al. 2021):

$$L_j \approx 1.7 \times 10^{45}\zeta^{3/2}\left(\frac{L_{151}}{10^{44}\ \mathrm{erg\ s^{-1}}}\right)^{6/7} \mathrm{erg\ s^{-1}}, \tag{12}$$

for 415 sources in our sample with available beam radio luminosity at 151 MHz. From the beam radio luminosity at 151 MHz, and adopting $\zeta = 1.0$, as in Cao (2003), we calculated the beam power and found that the logarithm of the beam power was in a range of 40.15–45.60 (erg $\mathrm{s^{-1}}$), with a mean value of 43.68 ± 1.01 (erg $\mathrm{s^{-1}}$) for the 415 blazars.

3.6. Black Hole Spin

Daly (2016) gave an empirical relationship related to the fundamental line of black hole activity, with beam power L_j, accretion disk bolometric luminosity $L_{\rm bol}$, and Eddington luminosity $L_{\rm Edd}$:

$$\frac{L_j}{L_{\rm bol}} \propto \left(\frac{L_{\rm bol}}{L_{\rm Edd}}\right)^{\rm A-1}, \tag{13}$$

where A is a constant. The accretion disk bolometric luminosity $L_{\rm bol}$ and the beam power L_j are easier to be parameterized, in the form of general equations that can be combined together to solve for the spin function $f(j)$ in his paper. In this case, the beam power and accretion disk bolometric luminosity need to be parameterized as maximum possible values ($L_{\rm bol}$ (max) and L_j (max)). From Equations (4) and (5), Daly (2016, 2019) rewrote the black hole spin function, $f(j)$, as follows:

$$\frac{f(j)}{f_{\rm max}} = \left(\frac{L_j}{g_j L_{\rm Edd}}\right)\left(\frac{L_{\rm bol}}{g_{\rm bol} L_{\rm Edd}}\right)^{-\rm A}, \tag{14}$$

Table 2
Classification Results

Model (1)	Class (2)	Component (3)	Mean (4)	st.de (5)	cro.po (6)	Probability (7)	N (8)
V	BL Lacs	left	−2.93	1.26	−2.43	0.417	150
V	FSRQs	right	−1.84	0.31		0.583	299
E	BL Lacs	left	−4.07	0.50	−3.14	0.193	88
E	FSRQs	right	−1.87	0.50		0.807	361

Note. Column (1): model, with a *V* model option and an *E* model option. Column (2): classification, with BL Lacs and FSRQs. Column (3): component, with a left component and a right component. Column (4): the mean values for each component. Column (5): the standard deviations for each component. Column (6): where the curves of the two components join at a crossing point. Column (7): the probability for each component. Column (8): the number for each component.

where j is the dimensionless black hole spin given by $j = Jc/(GM^2)$, where J is the black hole spin angular momentum; $f_{\rm max}$ is the maximum possible value of $f(j)$ corresponding to a dimensionless spin $j = 1$; and the beam power and accretion disk bolometric luminosity are parameterized with normalization factors as $L_{\rm bol}\,({\rm max}) = g_{\rm bol}\,L_{\rm Edd}$ and $L_j\,({\rm max}) = g_j\,L_{\rm Edd}$, where the dimensionless mass accretion rate $\dot{m} = 1$ and the dimensionless efficiency factors $\epsilon = 1$, $\dot{m}$, and ϵ appear in the general equations for $L_{\rm bol}$ and L_j from Daly (2016).

The Blandford–Znajek model and the Meier model suggest that the conversion from the spin function to the black hole spin is $\sqrt{f(j)/f_{\rm max}} = j(1 + \sqrt{1 - j^2})^{-1}$, allowing the black hole spin to be expressed as

$$j = \frac{2\sqrt{f(j)/f_{\rm max}}}{f(j)/f_{\rm max} + 1}, \tag{15}$$

for $f(j)/f_{\rm max} \leqslant 1$. Daly et al. (2018) presented $A \simeq 0.45 \pm 0.01$, from a best-fit of the fundamental line, and Daly (2019) adopted $g_{\rm bol} = 1$ and $g_j = 0.1$, but we use a substitute for the accretion disk bolometric luminosity, $L_{\rm bol} \approx 10 L_{\rm BLR}$ (Netzer 1990), and calculate the spin of the black hole with equations (14) and (15), obtaining the black hole spin as being in a range of 0.0168–0.9995, with a mean value of 0.46 ± 0.26 for 415 blazars.

4. Discussions

4.1. Separating BL Lacs and FSRQs

As shown in Figure 4, both the 1D and 2D methods give the same classifications, except for two sources (4FGL J0434.1–2014 and 4FGL J1015.0+4926), marked as the solid red stars, which are divided into the region of FSRQs by the 1D method, but into the region of BL Lacs by the 2D method. From the classification of 4FGL-DR2, we can see that some BL Lacs in 4FGL-DR2 are assigned to the region of FSRQs by both the 1D and 2D methods, and vice versa. Namely, from the classification of the 1D method, 39 BL Lacs in 4FGL-DR2 are located in the region of the FSRQ population (including the two BL Lacs mentioned above), and seven FSRQs in 4FGL-DR2 are located in the region of the BL Lac population. Based on the classification of the 2D method, 37 BL Lacs in 4FGL-DR2 are located in the region of the FSRQ population, and seven FSRQs in 4FGL-DR2 are located in the region of the BL Lac population. These blazars are indistinct to the dividing line, based on the 1D or 2D method, and these results provide some inspiration for us: maybe some blazars are changing-look blazars with broad emission-line turn-on (as FSRQs) or turn-off (as BL Lacs).

For nonjetted and general AGNs, if their X-ray slopes or their broad emission-line profiles and intensities change dramatically over time, they will be classified as changing-look AGNs due to the changes in obscuration, or the variations in the accretion rate, and thus ionizing luminosity, in a situation where there are only line variations. The type will change when the broad emission lines in the sight of the observer are obscured by moving clouds or the dust torus (Goodrich 1989), but this phenomenon cannot explain the strong changes of the infrared band or low polarization (Sheng et al. 2017; Hutsemékers et al. 2019). These changes may be due to tidal disruption events (TDEs; Merloni et al. 2015), but TDEs cannot explain the repeating changing-look AGNs. The variations in the accretion rate of the accretion disk may trigger changing-look AGN events (Sniegowska et al. 2020), but the timescale for the variations in the accretion rate far exceeds the observational timescale for changing-look AGNs. For jetted blazars, these are classified as changing-look blazars if they transfer their types between FSRQs and BL Lacs at different observational periods, and this potentially different process may be related to the variations, as the broad emission line is overwhelmed by the continuum from the nonthermal jet emission (Ghisellini et al. 2012; Peña-Herazo et al. 2021).

We think that some BL Lacs in 4FGL-DR2 are divided into the FSRQ population by both the 1D and 2D methods (and vice versa) due to their changing-look characteristics, and we can also obtain more evidence for changing-look blazars from the classifications in the different Fermi FGL catalogs. Now, we focus on the objects discussed above, and track the histories of their classification in the Fermi FGL catalogs (including 1FGL, 2FGL, 3FGL, and 4FGL/4FGL-DR2). If an object is labeled as a different subclass in different Fermi FGL catalogs, then it is recorded as a changing-look blazar in our sample. In this way, we find five changing-look blazars (4FGL J0114.8+1326: 1bzb/2bzq/3CB/4CB; 4FGL J0203.7+3042: 1agu/2bzq/3CB/4CB; 4FGL J0407.5+0741: 1bzq/2bzq/3CB/4CB; 4FGL J0433.1+3227: 1bzq/2bzq/3BCU/4CB; and 4FGL J1058.4+0133: 1bzq/2bzb/3CB/4CB). For example, 1bzb/2bzq/3CB/4CF means that this object is classified as a BL Lac in 1FGL (denoted as "bzb" from the text in 1FGL), is classified as an FSRQ in 2FGL (denoted as "bzq" from the text in 2FGL), is classified as a BL Lac in 3FGL (denoted as a CB in this work), and is classified as an FSRQ in 4FGL (denoted as a CF in this work); "agu" here means the active galaxies of uncertain type, from Nolan et al. (2012). Interestingly, these five sources are all distributed in the region of the FSRQ population; see Figure 4.

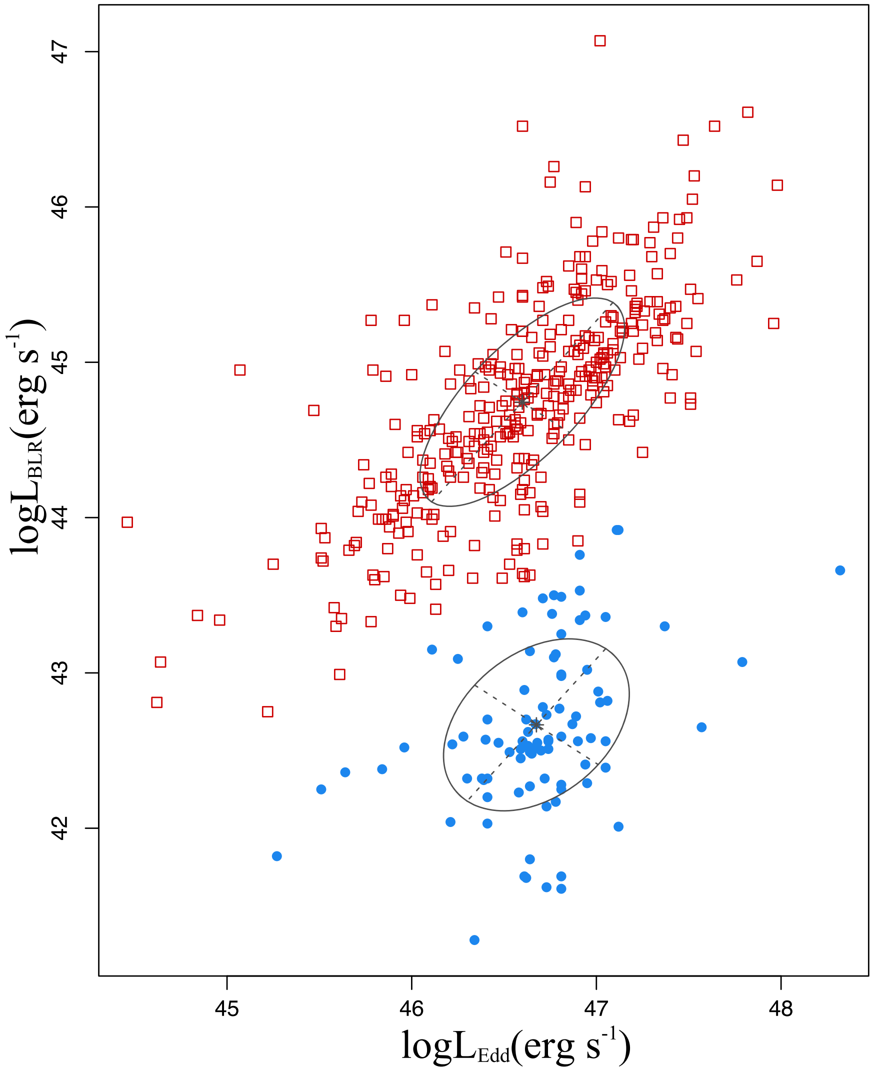

Figure 3. The GMM fit for 2D data. The 2D classification is based on the BLR luminosity and the Eddington luminosity. The solid blue circles represent the BL Lac population, with weak emission, and the hollow red squares represent the FSRQ population, with strong emission.

From the results of the comparison in Figure 4, both the 1D and 2D methods support the dividing line proposed in G11 ($L_{\rm BLR}/L_{\rm Edd} \sim 5 \times 10^{-4}$), which indicates that the FSRQs have more powerful BLR luminosities in units of Eddington luminosity than do the BL Lacs. Compared to the classification of the 2D method, we can utilize the result of the 1D method as a criterion for separating the BL Lacs and the FSRQs. One important point that should be stressed is that we still use the classifications for the BL Lacs and FSRQs labeled in 4FGL-DR2, and that the purpose of the classifications described by the 1D or 2D methods in this work is to divide the BCUs into candidates for FSRQs ("CFUs") and BL Lacs ("CBUs"). We label "CFs" as FSRQs and "CBs" as BL Lacs: "CFs" are the FSRQ population of the total FSRQs and CFUs, "CBs" are the BL Lac population of the total BL Lacs and CBUs, and "CLs" are changing-look blazars in this paper.

4.2. Black Hole Masses

4.2.1. Comparisons of Black Hole Masses

Narrowline Seyfert 1 galaxies (NLS1s) are also a subclass of AGNs with powerful relativistic jets, and γ-ray emissions from three radio-loud NLS1s have been detected by Fermi LAT, as well as blazars and radio galaxies (Abdo et al. 2009). However, we did not calculate the black hole masses for the NLS1s, because the physical characteristics of the NLS1s are different from those of blazars and radio galaxies. For examples, the NLS1s are hosted in spiral galaxies (Crenshaw et al. 2003), while the blazars and radio galaxies are hosted in elliptical galaxies (Sikora et al. 2007), and the black hole masses of NLS1s are lower than those of blazars and radio galaxies, which is possibly caused by the inclination projection effect described in Chen et al. (2018), therefore we focus on blazars in this work, even though NLS1s have powerful relativistic jets as blazars. Based on the reverberation technique (Wandel et al. 1999; Kaspi et al. 2000), the estimated black hole masses are distributed over a range of $10^{7}-10^{8}\,M_{\odot}$ for 17 Seyfert 1 galaxies and over a range of $10^{8}-10^{9}\,M_{\odot}$ for 17 quasars. Based on the minimum variability timescale, Xie et al. (2004) estimated black hole masses over a range of $10^{7.2}-10^{9.4}\,M_{\odot}$ for 39 blazars. In the present sample of 449 blazars, their black hole masses are in a range of $10^{6.35}-10^{10.21}\,M_{\odot}$. It is also obvious that there are six blazars (4FGL J0217.0–0821, 4FGL J0217.4+7352, 4FGL J0430.3–2507, 4FGL J0910.0+4257, 4FGL J1625.7+4134, and 4FGL J1954.6–1122) in our sample whose black hole masses, as derived from the lines of

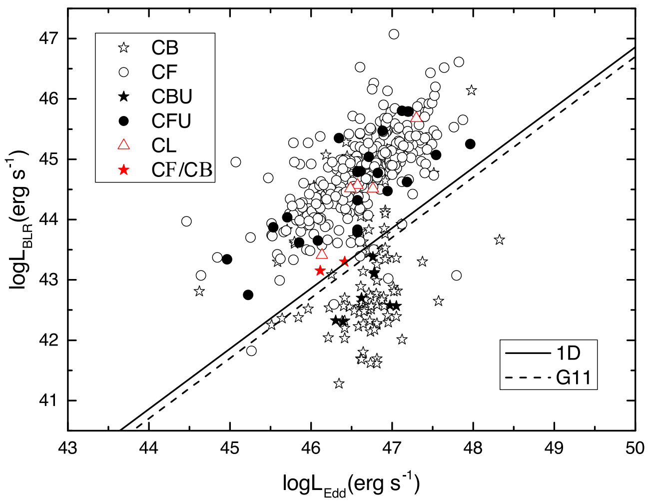

Figure 4. Comparisons among three different methods for the classification of blazars. The hollow black stars represent BL Lacs (CB), the hollow black circles represent FSRQs (CF), the solid black stars represent BCUs separated into the BL Lac population (CBUs), the solid black circles represent BCUs separated into the FSRQ population (CFUs), the hollow red triangles represent changing-look blazars (CLs), and the solid red stars represent BL Lacs that are separated as FSRQs by the 1D method, but are separated as BL Lacs by the 2D method. The solid black solid line represents the classification result from the 1D method, and the black dashed line represents the classification result from G11.

H β/Mg II/C IV in the available literature, are smaller than $10^7\,M_\odot$, and one blazar, 4FGL J2134.2-0154, whose black hole mass, as derived from the magnitude, is more massive than $10^{10}\,M_\odot$.

To test whether our complements to the black hole masses of some sources are correct and reasonable, we compared the black hole masses in the following categories. For the whole sample in this work (449 objects), we used CO for blazars with available masses from continuum emissions (307 objects), TW for blazars whose masses we calculated using BLR emissions in this work (72 objects), and OM for blazars whose masses were calculated from other methods, including empirical formulae, in the available literature (48 objects); see Table 1 for the details of each category. A Kolmogorov–Smirnov (K–S) test was done for pairs of each of the specified categories, the null hypothesis being that the two categories specified were drawn from the same distribution, with the statistic value $D_{\rm KS}$ being the maximum separation of the cumulative fractions of the two categories. The results show that the significant level probability is $p_{\rm KS} = 0.11$ with $D_{\rm KS} = 0.16$ for TW–CO and $p_{\rm KS} = 0.01$ with $D_{\rm KS} = 0.30$ for TW–OM, suggesting that the distribution of the black hole masses that we calculated in this work (TW) is similar to that of the available ones (CO), but different from the distribution of the black hole masses calculated from other methods (OM), because both TW and CO use the same method, with BLR or continuum emissions, but TW and OM use different methods, and, of course, there are different sources of error. In spite of this, the distribution of the black hole masses of 72 blazars (66 FSRQs, five BL Lacs, and one CFU) that we estimated is reasonable; see the distributions with probability densities in Figure 5.

4.2.2. Error Sources of Estimations for Black Hole Masses

We consider the drawbacks of this virial method for black hole mass estimation. First of all, the different versions of the calibration have an influence on the coefficients a_* and b_* in Equation (4): MD04 adopted the old version of reverberation-based black hole mass and virial coefficients to calibrate the broad lines of Hβ and MgII, while others (e.g., VP06; Vestergaard & Osmer 2009) have adopted the updated version of reverberation-based black hole mass and virial coefficients, from Onken et al. (2004), for the calibration. Second, the broad emission for deriving the size of the BLR, and the measurement of the FWHM for the velocity of the BLR, both directly affect the value estimated for the black hole mass, and it is straightforward to estimate the virial black hole mass by simplifying the properties of the broad lines. Six blazars with black hole masses smaller than $10^7\,M_\odot$, collected from the literature, perhaps have smaller FWHM measurements. Last but not least, the continuum luminosity would be contaminated by the effects of the synchrotron radiation from the jet, the dust, and the host galaxy of the AGN (Oshlack et al. 2002), where the obscurity of the dust is likely to reduce the continuum luminosity, while the enhancements of the jet synchrotron radiation and the host galaxy may be the reason why the object with a black hole mass that was estimated from the magnitude was larger than $10^{10}\,M_\odot$.

In summary, for jetted sources (including blazars), the continuum luminosity, which is more or less significantly contaminated by the jet continuum, and the FWHM, which depends on the accretion luminosity and the inclination of the disk, are not better options for estimating the central black hole mass, but a large majority of our sample was directly obtained from S12, who also use the virial method; their black hole masses provided useful references for our calculation results in this work, but we still adopted the method outlined in Equations (5)–(8) to estimate the black hole masses of 72 blazars.

4.2.3. Correlations between γ-Ray Luminosity and Black Hole Masses

The relativistic beaming effect causes an enhancement to the emissions from the jet in the observer's frame: $F^{\rm ob} = \delta^k\,F^{\rm in}$, where $F^{\rm ob}$ is the observed emission, $F^{\rm in}$ is the intrinsic emission, δ is the Doppler factor, which can be calculated as in Zhang et al. (2020), and k is the value related to the shape of the emission spectrum and the detailed physics of the jet (Lind & Blandford 1985), so that $k = 2 + \alpha$ for a continuous jet and $k = 3 + \alpha$ for a discrete jet. The relation between black hole mass and radio luminosity has been investigated in earlier works (Lacy et al. 2001; Oshlack et al. 2002; McLure & Jarvis 2004), but we have revisited this relation using observed and intrinsic γ-ray luminosities in this work, with the scatter diagrams being shown in Figures 6(a), (b), and (c). The black hole mass is weakly correlated with the observed γ-ray luminosity from the BISECTOR fit of ordinary and symmetrical least-squares (OLS; Feigelson & Babu 1992) for the whole sample:

$$\log L_\gamma = (34.52 \pm 0.71) + (1.37 \pm 0.08)\log M, \qquad (16)$$

with a correlation coefficient $r_{\rm P} = 0.21$ and a significant level probability $p_{\rm P} < 10^{-4}$ from a Pearson regression, $r_{\rm S} = 0.23$ and $p_{\rm S} < 10^{-4}$ from a Spearman regression, and $r_{\rm K} = 0.15$ and $p_{\rm K} < 10^{-4}$ from a Kendall regression, where all the p-values are smaller than 10^{-5}. For the continuous jet, the black hole mass is moderately correlated with the intrinsic γ-ray luminosity for the whole sample:

$$\log L_\gamma^{2\rm in} = (23.31 \pm 0.98) + (2.25 \pm 0.12)\log M, \qquad (17)$$

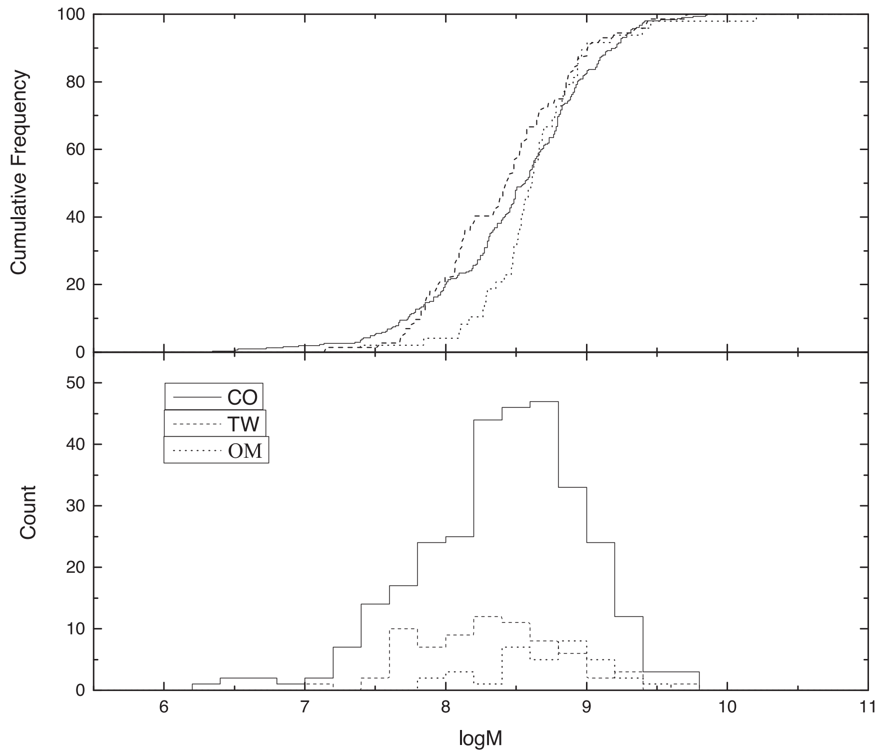

Figure 5. The lower panel shows the distributions of the black hole mass ($\log M = \log(M_{\rm BH}/M_\odot)$): the solid line represents the distribution of the black hole masses estimated by continuum emissions for the available blazars (abbreviated as CO), the dashed line represents the distribution of the black hole masses of the blazars that we calculated in this work (abbreviated as TW), and dotted line represents the distribution of the black hole masses of the blazars that were calculated by other methods (abbreviated as OM). The upper panel shows the cumulative frequency distributions for the corresponding distributions of CO, TW, and OM.

with $r_{\rm P} = 0.51$ and $p_{\rm P} < 10^{-4}$ from a Pearson regression, $r_{\rm S} = 0.48$ and $p_{\rm S} < 10^{-4}$ from a Spearman regression, and $r_{\rm K} = 0.34$ and $p_{\rm K} < 10^{-4}$ from a Kendall regression, where all the p-values are smaller than 10^{-27}. For the discrete jet, this relation is also moderate for the whole sample:

$$\log L_\gamma^{\rm 3in} = (19.09 \pm 1.30) + (2.65 \pm 0.15)\log M, \tag{18}$$

with $r_{\rm P} = 0.47$ and $p_{\rm P} < 10^{-4}$ from a Pearson regression, $r_{\rm S} = 0.44$ and $p_{\rm S} < 10^{-4}$ from a Spearman regression, and $r_{\rm K} = 0.31$ and $p_{\rm K} < 10^{-4}$ from a Kendall regression, where all the p-values are smaller than 10^{-22}.

As shown in Figures 6(a), (b), and (c), one can see the distributions of black hole mass and γ-ray luminosity. Whether the distribution of the BL Lac population (CBs) is similar to the distribution of the FSRQ populations (CFs) is something that needs to be tested. We used a new multivariate two-sample test, called the Cramér Test, included in the R package "cramer," to conduct the statistical test. The Cramér-statistic $T_{m,n}$ is given by:

$$T_{m,n} = \frac{mn}{m+n}\left(\frac{2}{mn}\sum_{i,j}^{m,n}\phi(\|\vec{X}_i - \vec{Y}_j\|^2) - \frac{1}{m^2}\sum_{i,j}^{m}\phi(\|\vec{X}_i - \vec{X}_j\|^2) - \frac{1}{n^2}\sum_{i,j}^{n}\phi(\|\vec{Y}_i - \vec{Y}_j\|^2)\right), \tag{19}$$

where the function ϕ is a kernel function, defined by default as

$$\phi_{Cramer}(x_i) = \frac{\sqrt{x_i}}{2}, \tag{20}$$

m is the number of observations in x sample and n is that in y sample, $\vec{X}_i$ denotes the ith observation in x sample, and $\vec{Y}_j$ denotes the jth observation in y sample. For the calculation of the critical value, a permutation of the Monte Carlo bootstrap method is chosen. More details about the test can be found in the cookbook for the R package "cramer" and the references therein (e.g., Baringhaus & Franz 2004).

First, the Cramér Test for the distributions of log M and log L_γ in the CB sample and in the CF sample is performed. There are 120 observations in the CB sample and 329 observations in the CF sample. The observed Cramér-statistic is 35.96, which is higher than the critical value of 1.84 for the 95% confidence level, and the estimated p-value is extremely close to 0. Therefore, the distributions of log M and log L_γ in the CB sample are not similar to those in the CF sample. Next, the Cramér Test for the distributions of log M and log L_γ^{2in} in the CB sample and in the CF sample is performed. The number of observations in the CB sample is 120 and there are 329 observations in the CF sample. The observed Cramér-statistic is 4.60, which is nearly twice the critical value of 2.00 for the 95% confidence level, and the estimated p-value is 0. Thus, the distributions of log M and log L_γ^{2in} in the CB sample are still different from those in the CF sample, but not as extreme as in the first test. Last, the distributions of log M and log L_γ^{3in} in the CBs and in the CFs are also tested, with 120 observations for the CBs and 329 observations for the CFs. The observed

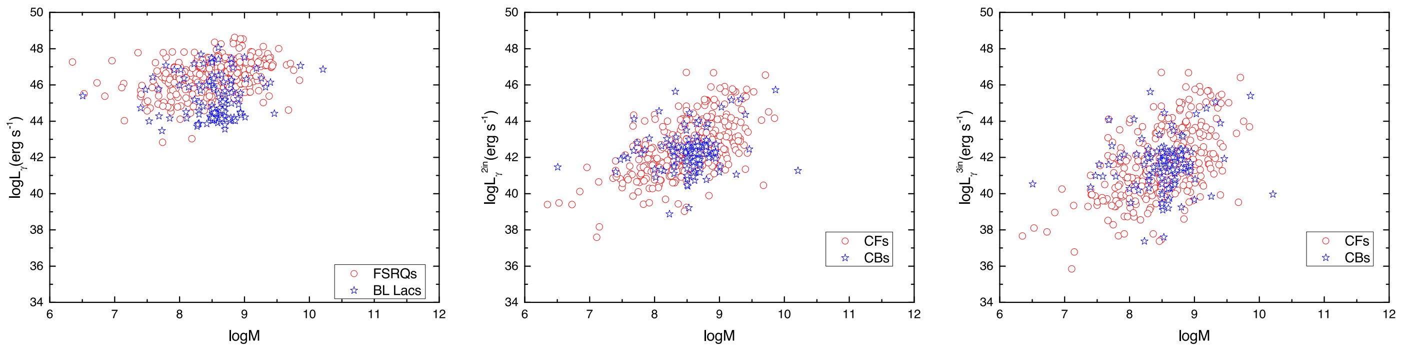

Figure 6. Scatter diagrams of the relation between γ-ray luminosity and black hole mass. The blue star symbols represent the BL Lac population (CBs) and the red circle symbols represent the FSRQ population (CFs). The left panel shows the correlation between the observed γ-ray luminosity and the black hole mass. The middle panel shows the correlation between the intrinsic γ-ray luminosity of continuous jets and the black hole mass. The right panel shows the correlation between the intrinsic γ-ray luminosity of discrete jets and the black hole mass.

Table 3
Linear Regression Results from OLS Fitting

Y (1)	X (2)	Class (3)	N (4)	$n \pm \Delta n$ (5)	$m \pm \Delta m$ (6)	r_P (7)	p_P (8)	r_S (9)	p_S (10)	r_K (11)	p_K (12)
$\log L_\gamma$	$\log M$	CFs	329	35.36 ± 0.62	1.31 ± 0.07	0.34	$p < 0.001$	0.34	<0.001	0.23	$p < 0.001$
$\log L_\gamma$	$\log M$	CBs	120	34.55 ± 1.88	1.26 ± 0.22	0.11	0.25	0.06	0.49	0.05	0.41
$\log L_\gamma^{2in}$	$\log M$	CFs	329	22.14 ± 0.98	2.40 ± 0.12	0.58	$p < 0.001$	0.57	$p < 0.001$	0.40	$p < 0.001$
$\log L_\gamma^{2in}$	$\log M$	CBs	120	29.99 ± 2.40	1.44 ± 0.28	0.19	0.04	0.13	0.15	0.09	0.15
$\log L_\gamma^{3in}$	$\log M$	CFs	329	17.37 ± 1.27	2.86 ± 0.15	0.54	$p < 0.001$	0.51	$p < 0.001$	0.36	$p < 0.001$
$\log L_\gamma^{3in}$	$\log M$	CBs	120	28.51 ± 3.29	1.53 ± 0.39	0.16	0.07	0.14	0.13	0.10	0.12
$\log P_{\rm jet}$	$\log L_{\rm disk}$	CFs	266	9.97 ± 2.12	0.80 ± 0.05	0.51	$p < 0.001$	0.49	$p < 0.001$	0.36	$p < 0.001$
$\log P_{\rm jet}$	$\log L_{\rm disk}$	CBs	89	-1.42 ± 3.43	1.07 ± 0.08	0.53	$p < 0.001$	0.58	$p < 0.001$	0.41	$p < 0.001$
$\log P_{\rm jet}$	$2\log j + 3\log M$	CFs^{co}	274	34.69 ± 1.08	0.47 ± 0.04	0.37	$p < 0.001$	0.40	$p < 0.001$	0.29	$p < 0.001$
$\log P_{\rm jet}$	$2\log j + 3\log M$	CBs^{co}	56	29.19 ± 2.02	0.67 ± 0.08	0.58	$p < 0.001$	0.54	$p < 0.001$	0.39	$p < 0.001$
$\log P_{\rm jet}$	$\log M$	CFs	266	38.44 ± 0.35	0.93 ± 0.04	0.37	$p < 0.001$	0.40	$p < 0.001$	0.28	$p < 0.001$
$\log P_{\rm jet}$	$\log M$	CBs	89	37.17 ± 1.43	1.04 ± 0.17	0.02	0.85	-0.03	0.82	-0.02	0.79
$\log P_{\rm jet}$	$\log j$	CFs	249	47.01 ± 0.05	1.87 ± 0.14	0.35	$p < 0.001$	0.40	$p < 0.001$	0.29	$p < 0.001$
$\log P_{\rm jet}$	$\log j$	CBs	81	47.78 ± 0.13	3.08 ± 0.17	0.78	$p < 0.001$	0.77	$p < 0.001$	0.56	$p < 0.001$

Note. Column (1): dependent variable. Column (2): independent variable. Column (3): classification. Column (4): the number of each classification; "CFs" indicates the total of the FSRQ, CFU, and named FSRQ populations; "CBs" indicates the total of the BL Lac, CBU, and named BL Lac populations; "CFs^{co}" indicates the compound CFs—the CFs plus the blazars of "CB-CF" and "CB-CF/CB," but minus the blazars of "CF-CB"; and "CBs^{co}" indicates the compound CBs—the CBs plus the blazars of "CF-CB," but minus the blazars of "CB-CF" and "CB-CF/CB" (see "CB-CF," "CB-CF/CB," and "CF-CB" from Table 1). Column (5): intercept and uncertainty. Column (6): slope and uncertainty. Column (7): correlation coefficient from Pearson. Column (8): chance probability from Pearson. Column (9): correlation coefficient from Spearman. Column (10): chance probability from Spearman. Column (11): correlation coefficient from Kendall. Column (12): chance probability from Kendall.

Cramér-statistic is 3.53, which is more than the critical value of 2.46 for the 95% confidence level, and the estimated p-value is 0.012. The possibility of the observations of the CBs being distributed like the observations of the CFs is rejected.

The correlations of the CFs and CBs are listed in Table 3. From this and Figures 6(a), (b), and (c), we can see that the CFs have a stronger correlation between the observed (as well as the intrinsic) γ-ray luminosity and the black hole mass than do the CBs. For both the CBs and the CFs, the correlation between the intrinsic γ-ray luminosity and the black hole mass is slightly stronger than that between the observed γ-ray luminosity and the black hole mass. This suggests that the black hole mass is more closely related to the intrinsic luminosity than the observed luminosity. As for the reason for the weak correlation between the observed γ-ray luminosity and the black hole mass, we think that it comes from the beaming effect, since the observed γ-ray luminosity (L_γ) is boosted by the beaming effect, $L^{\rm ob} = \delta^{k+1} L^{\rm in}$ ($F^{\rm ob} = \delta^{k} F^{\rm in}$). If the beaming effect (i.e., the Doppler factor) is different for different sources, then the amplifications of the observed γ-ray luminosity will vary for each source in the sample, meaning that the observed γ-ray luminosity will reduce its correlation with the black hole mass.

4.3. Mechanisms of Jet Formation

We collected the jet power SED from Chen (2018) and obtained the beam power from the beam radio luminosity for our sample, then drew a comparison between these two kinds of powers. The distributions and probability densities between these two kinds of powers are shown in Figure 7. We can see from Figure 7 that the K–S test gives a significant level probability of $p_{\rm KS} < 0.001$, with a maximum separation of the cumulative fractions $D_{\rm KS} = 0.70$, which means that the distribution of the jet power SED and that of the beam power are drawn from different distributions. The derived beam power is an average over a long timescale, as million of years are required to excavate for cavities, while the obtained jet power SED strongly depends on the γ-ray luminosity, and the γ-ray emission that dominates the energy output is based on short timescales, which are much shorter than

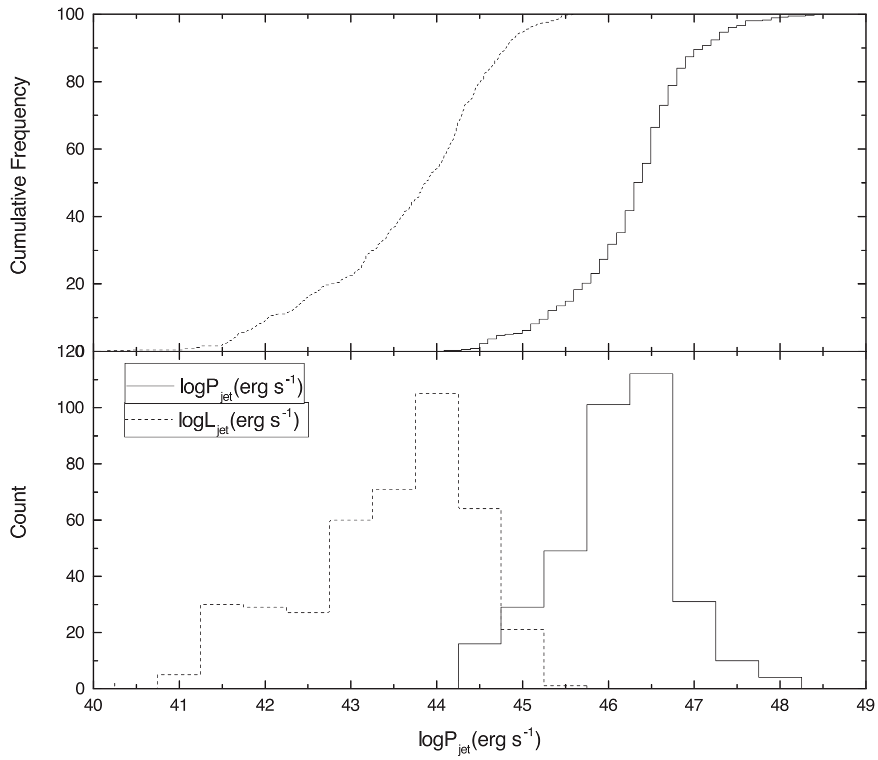

Figure 7. The lower panel shows the distributions of the logarithm of the jet power: the solid line represents the jet power SED ($\log P_{\rm jet}$) obtained from Chen (2018) and the dotted line represents the beam power ($\log L_{\rm jet}$ or $\log L_{\rm j}$) calculated from the beam radio luminosity. The upper panel shows the cumulative frequency distributions for these two kinds of jet powers.

those at radio frequencies, such as days, weeks, months, or even years, if we consider the average timescale from the LAT catalogs. Therefore, the jet power derived from the SED will always be much greater than the beam power derived from the beam radio luminosity at low frequency.

4.3.1. Jet–Disk Connection

Ghisellini (2006) considered that the Pointing flux is the driving energy of relativistic jets, so the Blandford–Znajek power (Blandford & Znajek 1977) is constrained under some assumptions:

$$L_{\rm BZ} \sim 6 \times 10^{20}\left(\frac{a_{\rm J}}{m}\right)^2\left(\frac{M_{\rm BH}}{M_\odot}\right)^2 B^2 \text{ erg s}^{-1}, \tag{21}$$

where $\frac{a_{\rm J}}{m}$ ($\equiv j$) is the specific angular momentum of the black hole, with $\frac{a_{\rm J}}{m} \sim 1$ for a maximum rotating black hole, $a_{\rm J}$ is defined as $a_{\rm J} \equiv J/(Mc)$, $m \equiv GM/c^2$ is the gravitational radius of the black hole, and B is the magnetic field in units of Gauss. As a small portion (ϵ_B) of the energy from gravitation, the magnetic energy density $\left(U_B = \frac{B^2}{8\pi}\right)$ in the vicinity of the black hole is expressed as:

$$U_B = \epsilon_{\rm B}\frac{GM_{\rm BH}\rho}{R} = \epsilon_{\rm B}\frac{R_s}{R}\frac{\rho c^2}{2}. \tag{22}$$

$R_s = \frac{2GM_{\rm BH}}{c^2}$ is the Schwarzschild radius, R is the stellar radius, ρ is linked to the accretion rate—$\dot{M} = 2\pi\, R\, H\, \rho\beta_{\rm R}\, c$, H is the disk thickness, $\beta_{\rm R}c$ is the radial infalling velocity, and the disk luminosity is$L_{\rm disk} = \eta_{\rm acc}\dot{M}c^2$, with $\eta_{\rm acc}$ being the accretion efficiency. The Blandford–Znajek power is then:

$$L_{\rm BZ} \sim \left(\frac{a_{\rm J}}{m}\right)^2\frac{R_s^3}{R^2 H}\frac{\epsilon_{\rm B}}{\eta_{\rm acc}}\frac{L_{\rm disk}}{\beta_{\rm R}}, \tag{23}$$

and when $R \sim H \sim R_{\rm s}$, $\frac{a_{\rm J}}{m} \sim 1$, $\epsilon_{\rm B} \sim 1$, and $\beta_{\rm R} \sim 1$, the maximum jet power is as follows (Ghisellini 2006):

$$L_{\rm BZ,max} \sim \frac{L_{\rm disk}}{\eta_{\rm acc}}. \tag{24}$$

Therefore, there is a link that directly connects the jet power and the disk luminosity, which is studied extensively in the literature (Celotti et al. 1997; Cao & Jiang 1999; Sbarrato et al. 2012; Ghisellini et al. 2014; Xiong & Zhang 2014; Zhang et al. 2020). The correlation between the jet power and the disk luminosity is moderately strong, and it shows the OLS BISECTOR fit for our whole sample:

$$\log P_{\rm jet} = (11.76 \pm 1.47) + (0.76 \pm 0.03)\log L_{\rm disk}, \tag{25}$$

with $r_{\rm P} = 0.51$ and $p_{\rm P} < 10^{-4}$ from a Pearson regression, $r_{\rm S} = 0.43$ and $p_{\rm S} < 10^{-4}$ from a Spearman regression, and $r_{\rm K} = 0.32$ and $p_{\rm K} < 10^{-4}$ from a Kendall regression, where all the p-values are smaller than 10^{-17}. The scatter diagrams are shown in Figure 8, with the color bar indicating the black hole mass, and Figure 9, with the color bar indicating the black hole spin, respectively.

In Figures 8 and 9, the diagonal lines represent an equivalent relation of $P_{\rm jet} = L_{\rm disk}$, and almost all CBs have a much larger jet power than accretion disk luminosity, except for the four BL Lacs that lie below the diagonal line. The four objects are 4FGL J0325.5–5635, 4FGL J0433.1+3227 (we identified this as a changing-look blazar), 4FGL J0856.8+2056, and 4FGL

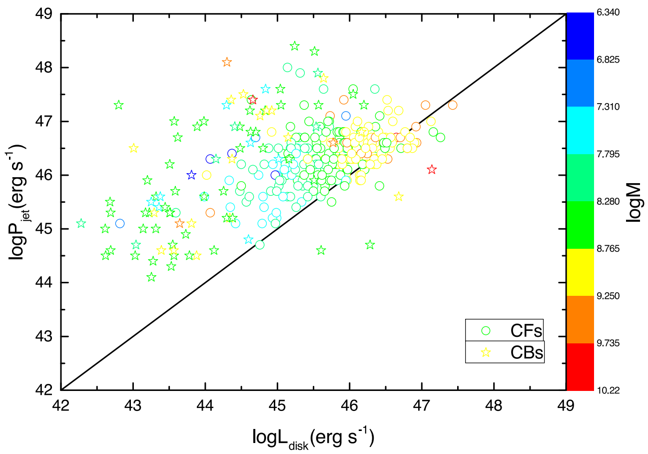

Figure 8. Scatter diagram between the jet power SED ($\log P_{\rm jet}$) and the disk luminosity ($\log L_{\rm disk}$). The diagonal line shows $\log P_{\rm jet} = \log L_{\rm disk}$, the color bar from blue to red shows the black hole mass from low to high, the stars represent the BL Lac population (CBs), and the circles represent the FSRQ population (CFs).

J2243.7–1231, and they are classified as FSRQs by our 1D and 2D methods in this work. The CFs are located closer to the diagonal line: a majority of the CFs have a slightly larger jet power than accretion luminosity, and a small number of CFs have a jet power that is slightly less than the accretion luminosity. Our results suggest that $P_{\rm jet} > L_{\rm disk}$ for almost all CBs, and $P_{\rm jet} \sim L_{\rm disk}$ for a larger number of CFs. The result for the CFs is in agreement with that from Chen (2018), who only studied FSRQs, due to the missing broadline emissions in BL Lacs.

The distributions of $\log L_{\rm disk}$ and $\log P_{\rm jet}$ in the CB sample and in the CF sample are also shown in Figures 8 and 9, and are used to perform the Cramér Test. There are 89 values for the CBs and 266 values for the CFs. The observed statistic is 45.57, the critical value for the 95% confidence level is only 1.64, and the estimated p-value is 0. These values mean that the distribution of the CBs is not similar to the distribution of the CFs.

Ghisellini (2006) provided interpretations for the different phenomena of FSRQs and BL Lacs similar to the above correlations: the jets in FR II radio galaxies (the parent population of the FSRQs) are powerful, and only a small fraction of their power needs to be dissipated to power the radio lobes, therefore the jet power in FR II radio galaxies (FSRQs) is comparable to their accretion disk luminosity (or slightly larger than when flaring). For most powerless FR I radio galaxies (the parent population of the BL Lacs), there are no strong broad emission lines manifesting the accretion disk luminosity, so the jet power in FR I radio galaxies (BL Lacs) is much larger than their accretion disk luminosity. Chen (2018) has also explained the phenomena of a considerable number of FSRQs: their jet power is greater than their accretion disk luminosity, and the ratio of their jet power to their accretion disk luminosity ($\log(P_{\rm jet}/L_{\rm disk})$) is greater than zero. This suggests that there are other ingredients, not only the accretion disk luminosity, for the launching of the jets, and that the jets in FSRQs may be dominated by the Blandford–Znajek process (Blandford & Znajek 1977).

4.3.2. Jet Launching

Daly (2009b) described and summarized the Blandford–Znajek model for the relationship among beam power (L_j), black hole mass (M), black hole spin (j), and magnetic field strength (B) in the form of

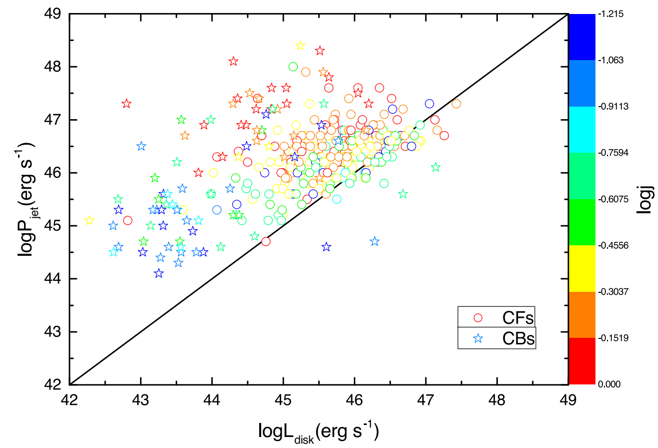

Figure 9. Scatter diagram between the jet power SED and the disk luminosity (as is described in Figure 8). The color bar from blue to red shows the black hole spin from low to high, the stars represent the BL Lac population (CBs), and the circles represent the FSRQ population (CFs).

$$L_j(BZ) \approx 2 \times 10^{43} j^2 M_8^2 B_4^2 \text{ erg s}^{-1}. \tag{26}$$

Using the relations of the Blandford–Znajek power mentioned above—$U_B = \frac{B^2}{8\pi}$, $R_s = \frac{2GM_{\rm BH}}{c^2}$, $\dot{M} = 2\pi\ RH\ \rho\ \beta_{\rm R}\ c$, $L_{\rm disk} = \eta_{\rm acc}\ \dot{M}\ c^2$, $B_4 \sim B_{p0}/(10^4 G)$, where $B_{p0} = \sqrt{30}\, B$ is the poloidal magnetic field strength at the horizon, obtained by comparing Equations (21) with (26), and using the jet power SED ($P_{\rm jet}$) instead of the beam power ($L_j(BZ)$—we can obtain:

$$\log P_{\rm jet} \approx 20.78 + 2\log j + 3\log M + \log L_{\rm disk} + \log\left(\frac{4G}{R^3 c^3 \eta_{\rm acc}}\right). \tag{27}$$

Equation (27) means that the accretion disk luminosity (related to the magnetic field strength), the central black hole mass, and the black hole spin all contribute to the jet power, supporting some theoretical works (e.g., Blandford & Znajek 1977; Meier 1999, 2001). But we hope to know how the jet power depends on the mass and the spin, and, for the two subclasses of blazars, whether there are differences in terms of the contributions to the jet power from the mass and the spin. Therefore, we investigate the correlation of the jet power ($\log P_{\rm jet}$) with the black hole mass and spin ($2\log j$ + $3\log M$) from Equation (27). We neglected $\log\left(\frac{4G}{R^3c^3\eta_{\rm acc}}\right)$, because it can be considered a canonical value, with $\eta_{\rm acc} = 0.1$ for the standard accretion mode (Ghisellini & Tavecchio 2008), or a maximum value of $\eta_{\rm acc} = 0.3$ from Thorne (1974). The OLS result shows a strong correlation for the whole sample:

$$\log P_{\rm jet} = (32.37 \pm 0.93) + (0.56 \pm 0.04)(2\log j + 3\log M), \tag{28}$$

with a coefficient $r_{\rm P} = 0.39$ and $p_{\rm P} < 10^{-4}$ from a Pearson regression, $r_{\rm S} = 0.46$ and $p_{\rm S} < 10^{-4}$ from a Spearman regression, and $r_{\rm K} = 0.32$ and $p_{\rm K} < 10^{-4}$ from a Kendall regression, where all the p-values are smaller than 10^{-13}. The scatter diagram is shown in Figure 10.

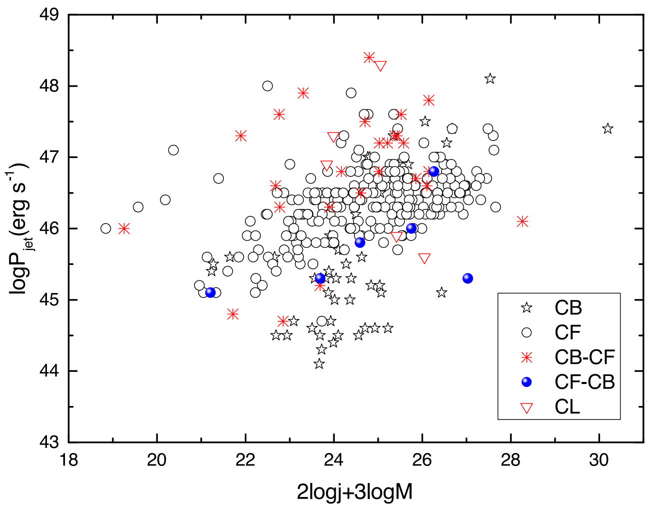

Figure 10. The correlation between the jet power ($\log P_{\rm jet}$) and the sum of the black hole mass and spin ($2\log j + 3\log M$). The hollow stars are the BL Lacs in 4FGL-DR2; the blue spherical symbols are the FSRQs in 4FGL-DR2 that are divided into BL Lacs by the 1D method; the hollow circles are the FSRQs in 4FGL-DR2; the red star symbols are the BL Lacs in 4FGL-DR2 that are divided into FSRQs by the 1D method; and the hollow red triangles are changing-look blazars. Based on the classification results of the 1D method, the BL Lac population (CBs) here includes the BL Lacs that are marked with hollow stars and blue spherical symbols, and the FSRQ population (CFs) here includes the FSRQs that are marked with hollow circles and red star symbols.

In Figure 10, the Cramér Test is also used to check whether the distributions of the two samples are similar. There are 81 observations of CBs and 249 observations of CFs. The observed statistic of 6.51 is obtained, which is larger than the 95% critical value of 2.37, and the estimated p-value is almost 0. The distribution of the CBs is different from that of the CFs.

For the subclasses, we noted that some BL Lacs are classified as FSRQs by the 1D method, which are marked with the red star symbols in Figure 10, and show a similar correlation tendency as the FSRQs. At the same time, some FSRQs are classified as BL Lacs by the 1D method, which are marked with the blue spherical symbols in Figure 10, and also show a similar correlation tendency as the BL Lacs. In this sense, we take the FSRQs and those BL Lacs (denoted by the red star symbols in Figure 10) that are classified as FSRQs by the 1D method as compound FSRQs, and denote them as CFs$^{\rm co}$; and we take the BL Lacs and those FSRQs (denoted by the blue spherical symbols in Figure 10) that are classified as BL Lacs by the 1D method as compound BL Lacs, and denote them as CBs$^{\rm co}$. We then investigate the correlation, as in Equation (28), for the two compound subclasses; the corresponding correlation results are listed in Table 3. It is found that the jet power is correlated with the sum of the black hole mass and black hole spin for the two compound subclasses, and that compound BL Lacs show a strong trend that is similar to the that of the compound FSRQs. Based on the above correlation for the compound BL Lacs, and the correlation between jet power and disk luminosity for BL Lacs, we infer that both the black hole mass and black hole spin have a great impact on the jet power, as well as the disk luminosity, implying that it is not only the accretion disk luminosity that contributes to BL Lacs. From the results of this work, the jets of BL Lacs tend to be dominated by the Blandford–Znajek process, in the contributions of both the black hole mass and black hole spin, similar to those of the FSRQs in the literature (Chen 2018). However, we cannot exclude the Blandford–Payne process, since the jet power is also correlated with the disk luminosity in BL Lacs, as shown in Figures 8 and 9.

Furthermore, according to the dividing result of $\log(L_{\rm BLR}/L_{\rm Edd})$, we found five changing-look blazars when we checked our classifications using the dividing line with the classifications in the Fermi FGL catalogs. We noted that some of the BL Lacs classified into FSRQs (CB-CFs) followed the sequence of FSRQs, and that some of the FSRQs classified into BL Lacs (CF-CBs) followed the sequence of BL Lacs. We propose that these ambiguous blazars (CB-CFs and CF-CBs) from the 1D method are candidates for changing-look blazars. We list these candidates for changing-look blazars in Table 4, and it is an issue worthy of follow-up research.

4.3.3. Correlations with Jet Power

For the correlation between jet power and disk luminosity, Figure 8 shows that the black hole mass (in color) makes little difference to it, while Figure 9 shows that the black hole spin (in color) has a trend that follows this correlation. Since the black hole mass and the black hole spin may make contributions to the jet power in the Blandford–Znajek model, as supported by Figure 10, we cannot ignore them and should discuss their influences. In addition, Liu et al. (2006) found an important intrinsic correlation between jet power and black hole mass, even when the relativistic beaming effect was eliminated from the radio and optical emissions, indicating that the jet formation is closely related to the black hole mass. The weaker correlation between jet power and black hole mass shows the OLS fit for the whole sample:

$$\log P_{\rm jet} = (36.81 \pm 0.32) + (1.11 \pm 0.04)\log M, \qquad (29)$$

with a correlation coefficient $r_{\rm P} = 0.20$ and $p_{\rm P} < 0.0002$ from a Pearson regression, $r_{\rm S} = 0.26$ and $p_{\rm S} < 10^{-4}$ from a Spearman regression, and $r_{\rm K} = 0.18$ and $p_{\rm K} < 10^{-4}$ from a Kendall regression, where all the p-values are smaller than 0.0002. The stronger correlation between jet power and black hole spin shows the OLS fit for the whole sample:

$$\log P_{\rm jet} = (47.21 \pm 0.05) + (2.33 \pm 0.12)\log j, \qquad (30)$$

with a correlation coefficient $r_{\rm P} = 0.59$ and $p_{\rm P} < 10^{-4}$ from a Pearson regression, $r_{\rm S} = 0.56$ and $p_{\rm S} < 10^{-4}$ from a Spearman regression, and $r_{\rm K} = 0.41$ and $p_{\rm K} < 10^{-4}$ from a Kendall regression, where all the p-values are smaller than 10^{-27}. These results are shown in Figures 11 and 12, with the color bar indicating the accretion disk luminosity, and there are some discrepancies between the CFs and the CBs in both Figures 11 and 12.

The Cramér Test of the distributions of $\log M$ and $\log P_{\rm jet}$ in the two samples is applied. The CBs have 89 values and the CFs have 266 values. The results indicate that the observed statistic is 8.26, the 95% confidence level critical value is 1.22, and the estimated p-value is 0. Therefore, the CBs are not distributed as are the CFs. For the distributions of $\log j$ and $\log P_{\rm jet}$ in these two samples, there are 81 observed values for the CBs and 249 values for the CFs. The derived statistic is 10.24, which is higher than the critical value of 1.02 for the 95% confidence level, and the estimated p-value is nearly 0. The hypothesis that the CBs are distributed as are CFs is rejected.

Figure 11 shows a poor correlation between the jet power and the black hole mass with large dispersion, in the case of

Table 4
Changing-look Blazars and Candidates

Name (1)	OName (2)	z (3)	Class (4)	log $L_{\rm BLR}$ (5)	log $L_{\rm Edd}$ (6)
4FGL J1616.7+4107	B31615+412	0.267	CB-CF	43.60	45.80
4FGL J0428.6-3756	PKS 0426-380	1.111	CB-CF	44.04	46.71
4FGL J0430.3-2507	PMN 0430-2507	0.516	CB-CF	42.81	44.62
4FGL J0538.8-4405	PKS 0537-441	0.892	CB-CF	45.05	46.44
4FGL J0747.2+4529	B3 0745+453	0.192	CB-CF	44.34	46.65
4FGL J0811.4+0146	PKS 0808+019	1.148	CB-CF	43.62	46.61
4FGL J0854.8+2006	OJ 287	0.306	CB-CF	43.85	46.90
4FGL J1001.1+2911	GB6 J1001+2911	0.558	CB-CF	43.15	45.59
4FGL J1751.5+0938	4C+09.57	0.322	CB-CF	43.70	46.53
4FGL J1800.6+7828	S5 1803+78	0.680	CB-CF	44.56	46.03
4FGL J2032.0+1219	PKS 2029+121	1.215	CB-CF	43.81	45.70
4FGL J2315.6-5018	PKS 2312-505	0.808	CB-CF	43.63	45.79
4FGL J0334.2-4008	PKS 0332-403	1.357	CB-CF	43.83	46.71
4FGL J0629.3-1959	PKS 0627-199	1.724	CB-CF	44.05	46.61
4FGL J0644.6+6039	NVSS J064435+603849	0.832	CB-CF	45.11	47.44
4FGL J0856.8+2056	TXS 0853+211	2.098	CB-CF	46.12	47.98
4FGL J1132.7+0034	PKS B1130+008	1.633	CB-CF	44.64	46.91
4FGL J1440.0-1530	PKS 1437-153	2.642	CB-CF	45.20	46.60
4FGL J2152.5+1737	S3 2150+17	0.874	CB-CF	44.15	46.91
4FGL J2206.8-0032	PMN J2206-0031	1.053	CB-CF	43.80	46.61
4FGL J2247.4-0001	PKS 2244-002	0.949	CB-CF	44.10	46.91
4FGL J2353.7-3037	PKS 2351-309	0.737	CB-CF	43.63	46.64
4FGL J0749.7+7450	RX J0749.4+7451	1.629	CB-CF	45.07	46.18
4FGL J1022.4-4231	PMN J1022-4232	1.280	CB-CF	45.19	47.14
4FGL J2243.7-1231	RBS 1888	0.630	CB-CF	45.28	46.43
4FGL J1509.7+5556	SBS 1508+561	0.978	CB-CF	44.77	47.51
4FGL J1811.3+0340	NVSS J181118+034113	1.420	CB-CF	44.02	45.90
4FGL J0434.1-2014	TXS 0431-203	0.928	CB-CF/CB	43.15	46.11
4FGL J1015.0+4926	1H 1013+498	0.212	CB-CF/CB	43.30	46.41
4FGL J0203.7+3042	B2 0200+30	0.955	CB-CF-CL	43.41	46.13
4FGL J0407.5+0741	TXS 0404+075	1.133	CB-CF-CL	44.51	46.76
4FGL J1058.4+0133	PKS 1055+01	0.888	CB-CF-CL	44.52	46.48
4FGL J0433.1+3227	NVSS J043307+322840	2.011	CB-CF-CL	45.61	47.30
4FGL J0114.8+1326	GB6 J0114+1325	0.685	CB-CF-CL	44.55	46.57
4FGL J0516.7-6207	PKS 0516-621	1.300	CB-CF	44.41	46.34
4FGL J0325.5-5635	1RXS J032521.8-563543	0.862	CB-CF	44.61	46.79
4FGL J0438.9-4521	PKS 0437-454	2.017	CB-CF	44.24	46.61
4FGL J1224.9+4334	B3 1222+438	2.001	CB-CF	45.15	46.94
4FGL J1754.5-6425	PMN J1754-6423	1.255	CB-CF	44.16	46.64
4FGL J1125.9+2005	4C+20.25	0.133	CF-CB	41.82	45.27
4FGL J0833.9+4223	OJ 451	0.249	CF-CB	43.07	47.79
4FGL J1512.2+0202	PKS 1509+022	0.219	CF-CB	43.02	46.95
4FGL J1924.8-2914	PKS B1921-293	0.353	CF-CB	43.92	47.12
4FGL J1037.4-2933	PKS 1034-293	0.312	CF-CB	43.50	46.77
4FGL J1048.0-1912	PKS 1045-18	0.595	CF-CB	43.39	46.60
4FGL J1615.6+4712	B3 1614+473	0.199	CF-CB	42.59	46.28

Note. Column (1): the name from 4FGL-DR2. Column (2): the other name. Column (3): redshift (z). Column (4): the classifications resulting from the classifications in Section 3.2; "CB-CF" denotes the BL Lacs that are classified as FSRQs by both the 1D and 2D methods; "CF-CB" denotes the FSRQs that are classified as BL Lacs by both the 1D and 2D methods; "CB-CF/CB" denotes the BL Lacs that are classified as FSRQs by the 1D method, but classified as BL Lacs by the 2D method; and "CB-CF-CL" denotes the changing-look blazars that are responsible for the "CB-CF" cases. Column (5): logarithm of the BLR luminosity (log $L_{\rm BLR}$), in units of erg s^{-1}. Column (6): logarithm of the Eddington luminosity (log $L_{\rm Edd}$), in units of erg s^{-1}.

(This table is available in machine-readable form.)

CBs, and a moderate correlation in the case of CFs, with small dispersion. The theoretical work gives $P_{\rm jet} \propto B^2 M^2 j^2$, so one could expect the jet power to be positively correlated with black hole mass; but the correlation of the CBs shown in Figure 11 is not consistent with the theoretical prediction, so we speculate that the inconsistency is caused by the black hole mass determination methods used for BL Lacs. There are 89 BL Lacs in the study of the correlation between the jet power and the black hole mass: the black hole masses of 22 BL Lacs were estimated from velocity dispersion using an empirical formula of $M - \sigma$, the mass of one BL Lac was estimated from its magnitude $M - M_i$, and the others were estimated from continuum or broadline emissions. It is reasonable to think that the black hole masses for these 23 BL Lacs have been overestimated, since the overestimation on the $M - \sigma$ empirical formula may reach two orders of magnitudes

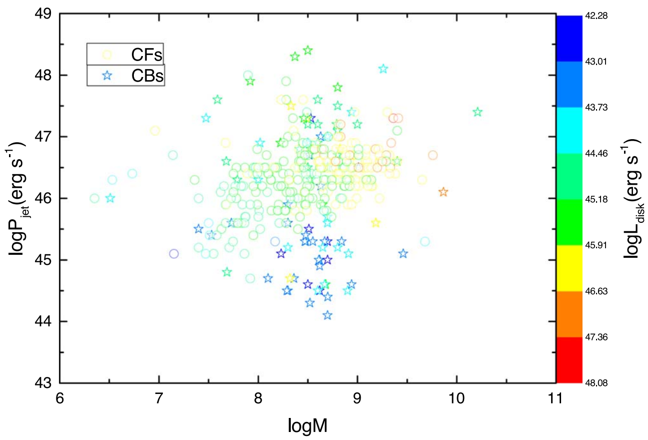

Figure 11. Scatter diagram between the jet power SED and the black hole mass. The color bar from blue to red shows the disk luminosity from low to high, the stars represent the BL Lac population (CBs), and the circles represent the FSRQ population (CFs).

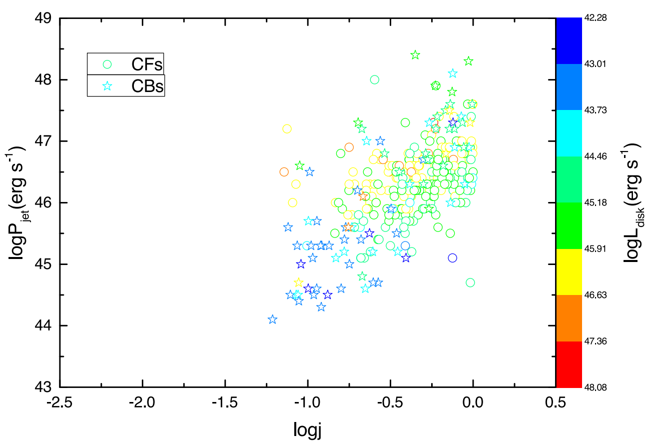

Figure 12. Scatter diagram between the jet power SED and the black hole spin. The color bar from blue to red shows the disk luminosity from low to high, the stars represent the BL Lac population (CBs), and the circles represent the FSRQ population (CFs).

(see Magorrian et al. 1998; Ferrarese & Merritt 2000), and the magnitudes from the continuum emissions may be contaminated by the jet (Oshlack et al. 2002). A possible solution is to reduce the overestimated black hole masses, but we do not know what fraction of black hole masses has been overestimated. Since the overestimation may reach two orders of magnitude, we will reduce the masses for those BL Lacs estimated using the empirical relationships of $M-\sigma$ and $M-M_i$ by one order of magnitude, and revisit the correlation between jet power and black hole mass. Using this approach, we found that the correlation became a tighter one, with higher confidence levels (p-values $<10^{-3}$ from a Pearson regression and a Spearman regression, and a p-value $\sim$0.001 for a Kendall regression). Therefore, the poor correlation between jet power and black hole mass for BL Lacs may be due to the different estimation methods used for the black hole masses.

Figure 12 shows a moderate correlation between jet power and black hole spin in the case of the CFs, and a strong correlation in the case of the CBs. Since the black hole spin for our sample is estimated using the beam power, black hole mass, and disk luminosity (a proxy for bolometric luminosity), from Equations (14)–(15), and since we can see that the correlation between jet power and black hole mass is not strong, and even weak for the CBs, we speculate that the strong correlation between jet power and black hole spin is mainly contributed by the disk luminosity (depending on the accretion luminosity). The correlation between jet power and black hole mass is moderate for the CFs, so we speculate that the moderate correlation between jet power and black hole spin is mainly contributed by the black hole mass (depending on the black hole mass), otherwise the correlation will be strong for CFs that are dominated by an accretion process. All the coefficients of the correlations of the CFs and CBs are listed in Table 3, and we compare the coefficients from a Pearson regression, a Spearman regression, and a Kendall regression.

5. Conclusions

In this paper, a large sample of 449 Fermi blazars with available BLR luminosities and black hole masses are compiled; their beam powers and black hole spins are estimated using the available beam radio emission detected by GMRT; and a dividing line between FSRQs and BL Lacs is revisited, through the ratio of the BLR luminosity to the Eddington luminosity, which aims to separate the BCUs in our sample. The relationship between black hole mass and γ-ray luminosity is discussed, with a consideration of the beaming effects of the relativistic jets. We reconsider the formation mechanism of the jets of AGNs by studying the correlations among jet power and disk luminosity, black hole mass, and black hole spin. Our conclusions are as follows.

1. In this work, the dividing line for classifying blazars into BL Lacs and FSRQs, obtained by the Bayesian analysis method, is of the order of log $(L_{\rm BLR}/L_{\rm Edd})$ $\sim$−3.14, which is consistent with the result in G11, and we found five changing-look blazars. In addition, the BL Lacs divided as FSRQs (or the FSRQs divided as BL Lacs) by log $(L_{\rm BLR}/L_{\rm Edd})$ are likely to be candidates for changing-look blazars.

2. A close correlation between black hole mass and intrinsic γ-ray luminosity is found, while only a weaker correlation is found between black hole mass and observed γ-ray luminosity. We think that the reason for this is due to the beaming effects of the jets.

3. The launching of relativistic jets is probably dominated by the Blandford–Znajek process, for both those FSRQs and BL Lacs with available broadline emissions.

4. The BL Lacs are mainly dominated by jets, while the FSRQs are mainly dominated by accretion processes. However, the jet power SED is weakly related to the black hole mass for BL Lacs with significant broad emissions, and their black hole spin turns out to be dominated by the accretion luminosity. The jet power SED is moderately related to the black hole mass for FSRQs, and their black hole spin turns out to be dominated by the mass.

We thank the anonymous referee for the useful comments and suggestions. The work is partially supported by the National Natural Science Foundation of China (NSFC U2031201 and NSFC 11733001) and the Natural Science Foundation of Guangdong Province (2019B030302001). We also acknowledge the science research grants from the China Manned Space Project, with NO. CMS-CSST-2021-A06, and the support from Astrophysics Key Subjects of Guangdong Province and Guangzhou City, as well as support that was also received from Guangzhou University (No. YM2020001).

ORCID iDs

Lixia Zhang https://orcid.org/0000-0003-3184-6896
Yi Liu https://orcid.org/0000-0003-3863-9777
Junhui Fan https://orcid.org/0000-0002-5929-0968

References

Abdo, A. A., Ackermann, M., Ajello, M., et al. 2009, ApJL, 707, L142
Abdo, A. A., Ackermann, M., Ajello, M., et al. 2010a, ApJ, 715, 429
Abdo, A. A., Ackermann, M., Ajello, M., et al. 2010b, ApJS, 188, 405
Acero, F., Ackermann, M., Ajello, M., et al. 2015, ApJS, 218, 23
Ackermann, M., Ajello, M., Atwood, W. B., et al. 2015, ApJ, 810, 14
Ajello, M., Angioni, R., Axelsson, M., et al. 2020, ApJ, 892, 105
Allen, S. W., Dunn, R. J. H., Fabian, A. C., Taylor, G. B., & Reynolds, C. S. 2006, MNRAS, 372, 21
Aschenbach, B., Grosso, N., Porquet, D., & Predehl, P. 2004, A&A, 417, 71
Baker, J. C., Hunstead, R. W., Kapahi, V. K., & Subrahmanya, C. R. 1999, ApJS, 122, 29
Baldwin, J. A., Wampler, E. J., & Burbidge, E. M. 1981, ApJ, 243, 76
Baldwin, J. A., Wampler, E. J., & Gaskell, C. M. 1989, ApJ, 338, 630
Ballet, J., Burnett, T. H., Digel, S. W., & Lott, B. 2020, arXiv:2005.11208
Baringhaus, L., & Franz, C. 2004, J. Multivar. Anal., 88, 190
Barth, A. J., Ho, L. C., & Sargent, W. L. W. 2003, ApJ, 583, 134
Bîrzan, L., McNamara, B. R., Nulsen, P. E. J., Carilli, C. L., & Wise, M. W. 2008, ApJ, 686, 859
Blandford, R. D., & Payne, D. G. 1982, MNRAS, 199, 883
Blandford, R. D., & Rees, M. J. 1978, in BL Lac Objects, ed. A. M. Wolfe (Pittsburgh, PA: Univ. Pittsburgh), 328
Blandford, R. D., & Znajek, R. L. 1977, MNRAS, 179, 433
Brotherton, M. S. 1996, ApJS, 102, 1
Brotherton, M. S., Wills, B. J., Steidel, C. C., & Sargent, W. L. W. 1994, ApJ, 423, 131
Browne, I. W. A., & Murphy, D. W. 1987, MNRAS, 226, 601
Cao, X. 2003, ApJ, 599, 147
Cao, X., & Jiang, D. R. 1999, MNRAS, 307, 802
Capelo, P. R., & Natarajan, P. 2007, NJPh, 9, 445
Cassaro, P., Stanghellini, C., Bondi, M., et al. 1999, A&AS, 139, 601
Cavagnolo, K. W., McNamara, B. R., Nulsen, P. E. J., et al. 2010, ApJ, 720, 1066
Celotti, A., Padovani, P., & Ghisellini, G. 1997, MNRAS, 286, 415
Chai, B., Cao, X., & Gu, M. 2012, ApJ, 759, 114
Chen, L. 2018, ApJS, 235, 39
Chen, S., Berton, M., La Mura, G., et al. 2018, A&A, 615, A167
Chen, Y., Gu, Q., Fan, J., et al. 2021, ApJ, 913, 93
Cheng, K. S., Fan, J. H., & Zhang, L. 1999, A&A, 352, 32
Corbin, M. R. 1992, ApJ, 391, 577
Crenshaw, D. M., Kraemer, S. B., & Gabel, J. R. 2003, AJ, 126, 1690
Crummy, J., Fabian, A. C., Gallo, L., & Ross, R. R. 2006, MNRAS, 365, 1067
Daly, R. A. 2009a, ApJL, 691, L72
Daly, R. A. 2009b, ApJL, 696, L32
Daly, R. A. 2011, MNRAS, 414, 1253
Daly, R. A. 2016, MNRAS, 458, L24
Daly, R. A. 2019, ApJ, 886, 37
Daly, R. A., Stout, D. A., & Mysliwiec, J. N. 2018, ApJ, 863, 117
di Serego Alighieri, S., Danziger, I. J., Morganti, R., & Tadhunter, C. N. 1994, MNRAS, 269, 998
Espey, B. R., Carswell, R. F., Bailey, J. A., Smith, M. G., & Ward, M. J. 1989, ApJ, 342, 666
Fabian, A. C., Vaughan, S., Nandra, K., et al. 2002, MNRAS, 335, L1
Falle, S. A. E. G. 1991, MNRAS, 250, 581
Fan, J. H. 2005, A&A, 436, 799
Fan, J. H., Xie, G. Z., & Bacon, R. 1999, A&AS, 136, 13
Fan, J. H., Yang, J. H., Yuan, Y. H., Wang, J., & Gao, Y. 2012, ApJ, 761, 125
Fan, J. H., Yang, J. H., Liu, Y., et al. 2016, ApJS, 226, 20
Fan, J. H., Yang, J. H., Xiao, H. B., et al. 2017, ApJL, 835, L38
Fan, J. H., Tao, J., Liu, Y., et al. 2018, AJ, 155, 90
Fan, J. H., Kurtanidze, S. O., Liu, Y., et al. 2021, ApJS, 253, 10
Fan, Z.-H., & Cao, X. 2004, ApJ, 602, 103
Fanaroff, B. L., & Riley, J. M. 1974, MNRAS, 167, 31P
Feigelson, E. D., & Babu, G. J. 1992, ApJ, 397, 55
Feng, H.-C., Liu, H. T., Bai, J. M., et al. 2021a, ApJ, 912, 92
Feng, H.-C., Hu, C., Li, S.-S., et al. 2021b, ApJ, 909, 18
Ferrarese, L., & Merritt, D. 2000, ApJL, 539, L9
Fraley, C., & Raftery, A. E. 2002, J. Am. Stat. Assoc., 97, 45
Fraley, C., Raftery, A. E., Murphy, T. B., & Scrucca, L. 2012, MCLUST Version 4 for R: Normal Mixture Modeling for Model-Based Clustering, Classification, and Density Estimation, Tech. Rep., No. 597
Francis, P. J., Hewett, P. C., Foltz, C. B., et al. 1991, ApJ, 373, 465
Fricke, K. J., Kollatschny, W., & Witzel, A. 1983, A&A, 117, 60
Gaskell, C. M., Shields, G. A., & Wampler, E. J. 1981, ApJ, 249, 443
Gelderman, R., & Whittle, M. 1994, ApJS, 91, 491
Genzel, R., Eckart, A., Ott, T., & Eisenhauer, F. 1997, MNRAS, 291, 219
Genzel, R., Schödel, R., Ott, T., et al. 2003, Natur, 425, 934
Ghisellini, G. 2006, VI Microquasar Workshop: Microquasars and Beyond, Vol. 27 (Trieste: PoS), 1
Ghisellini, G., & Tavecchio, F. 2008, MNRAS, 387, 1669
Ghisellini, G., Tavecchio, F., Foschini, L., & Ghirlanda, G. 2011, MNRAS, 414, 2674
Ghisellini, G., Tavecchio, F., Foschini, L., et al. 2012, MNRAS, 425, 1371
Ghisellini, G., Tavecchio, F., Maraschi, L., Celotti, A., & Sbarrato, T. 2014, Natur, 515, 376
Ghosh, P., & Abramowicz, M. A. 1997, MNRAS, 292, 887
Goodrich, R. W. 1989, ApJ, 340, 190
Greene, J. E., & Ho, L. C. 2005, ApJ, 630, 122
Gu, M., Cao, X., & Jiang, D. R. 2001, MNRAS, 327, 1111
Hartman, R. C., Bertsch, D. L., Bloom, S. D., et al. 1999, ApJS, 123, 79
Hunstead, R. W., Murdoch, H. S., & Shobbrook, R. R. 1978, MNRAS, 185, 149
Hutsemékers, D., Agís González, B., Marin, F., et al. 2019, A&A, 625, A54
Intema, H. T., Jagannathan, P., Mooley, K. P., & Frail, D. A. 2017, A&A, 598, A78
Jackson, N., & Browne, I. W. A. 1991, MNRAS, 250, 414
Junkkarinen, V. 1984, PASP, 96, 539
Kaspi, S., Smith, P. S., Netzer, H., et al. 2000, ApJ, 533, 631
Kinney, A. L., Huggins, P. J., Bregman, J. N., & Glassgold, A. E. 1985, ApJ, 291, 128
Komatsu, E., Smith, K. M., Dunkley, J., et al. 2011, ApJS, 192, 18
Lacy, M., Laurent-Muehleisen, S. A., Ridgway, S. E., Becker, R. H., & White, R. L. 2001, ApJL, 551, L17
Laor, A. 1998, ApJL, 505, L83
Lawrence, C. R., Zucker, J. R., Readhead, A. C. S., et al. 1996, ApJS, 107, 541
Li, S.-S., Yang, S., Yang, Z.-X., et al. 2021, ApJ, 920, 9
Liang, E. W., & Liu, H. T. 2003, MNRAS, 340, 632
Lind, K. R., & Blandford, R. D. 1985, ApJ, 295, 358
Liu, Y., Jiang, D. R., & Gu, M. F. 2006, ApJ, 637, 669
Magorrian, J., Tremaine, S., Richstone, D., et al. 1998, AJ, 115, 2285
Marziani, P., Sulentic, J. W., Dultzin-Hacyan, D., Calvani, M., & Moles, M. 1996, ApJS, 104, 37
McIntosh, D. H., Rieke, M. J., Rix, H. W., Foltz, C. B., & Weymann, R. J. 1999, ApJ, 514, 40
McLure, R. J., & Dunlop, J. S. 2001, MNRAS, 327, 199
McLure, R. J., & Dunlop, J. S. 2004, MNRAS, 352, 1390
McLure, R. J., & Jarvis, M. J. 2004, MNRAS, 353, L45
Meier, D. L. 1999, ApJ, 522, 753
Meier, D. L. 2001, ApJL, 548, L9
Meier, D. L. 2002, NewAR, 46, 247
Merloni, A., Dwelly, T., Salvato, M., et al. 2015, MNRAS, 452, 69
Merritt, D., & Ferrarese, L. 2001, MNRAS, 320, L30
Meyer, E. T., Fossati, G., Georganopoulos, M., & Lister, M. L. 2011, ApJ, 740, 98
Miley, G. 1980, ARA&A, 18, 165
Moderski, R., & Sikora, M. 1996, MNRAS, 283, 854
Morganti, R., Ulrich, M. H., & Tadhunter, C. N. 1992, MNRAS, 254, 546
Netzer, H. 1990, in Saas-Fee Advanced Course of the Swiss Society for Astrophysics and Astronomy: Active galactic nuclei, ed. R. D. Blandford et al. (Berlin: Springer), 57
Neugebauer, G., Oke, J. B., Becklin, E. E., & Matthews, K. 1979, ApJ, 230, 79
Nolan, P. L., Abdo, A. A., Ackermann, M., et al. 2012, ApJS, 199, 31
O'Dea, C. P., Daly, R. A., Kharb, P., Freeman, K. A., & Baum, S. A. 2009, A&A, 494, 471
Oke, J. B., Shields, G. A., & Korycansky, D. G. 1984, ApJ, 277, 64
Onken, C. A., Ferrarese, L., Merritt, D., et al. 2004, ApJ, 615, 645
Oshlack, A. Y. K. N., Webster, R. L., & Whiting, M. T. 2002, ApJ, 576, 81
Osmer, P. S., Porter, A. C., & Green, R. F. 1994, ApJ, 436, 678
Padovani, P. 1992, MNRAS, 257, 404
Panessa, F., Bassani, L., Cappi, M., et al. 2006, A&A, 455, 173
Peña-Herazo, H. A., Massaro, F., Gu, M., et al. 2021, AJ, 161, 196
Perez, E., Penston, M. V., & Moles, M. 1989, MNRAS, 239, 75
Peterson, B. M., Ferrarese, L., Gilbert, K. M., et al. 2004, ApJ, 613, 682
Pian, E., Falomo, R., & Treves, A. 2005, MNRAS, 361, 919

Plotkin, R. M., Markoff, S., Trager, S. C., & Anderson, S. F. 2011, MNRAS, 413, 805
Rawlings, S., & Saunders, R. 1991, Natur, 349, 138
Richstone, D. O., & Schmidt, M. 1980, ApJ, 235, 361
Rudy, R. J. 1984, ApJ, 284, 33
Sbarrato, T., Ghisellini, G., Maraschi, L., & Colpi, M. 2012, MNRAS, 421, 1764
Scarpa, R., Falomo, R., & Pian, E. 1995, A&A, 303, 730
Scrucca, L., Fop, M., & Murphy, T. B. 2016, The R Journal, 8, 205
Shaw, M. S., Romani, R. W., Cotter, G., et al. 2012, ApJ, 748, 49
Shen, Y., Richards, G. T., Strauss, M. A., et al. 2011, ApJS, 194, 45
Sheng, Z., Wang, T., Jiang, N., et al. 2017, ApJL, 846, L7
Sikora, M., Stawarz, Ł., & Lasota, J.-P. 2007, ApJ, 658, 815
Sitko, M. L., & Junkkarinen, V. T. 1985, PASP, 97, 1158
Smith, M. G., Carswell, R. F., Whelan, J. A. J., et al. 1981, MNRAS, 195, 437
Sniegowska, M., Czerny, B., Bon, E., & Bon, N. 2020, A&A, 641, A167
Steidel, C. C., & Sargent, W. L. W. 1991, ApJ, 382, 433
Stickel, M., Fried, J. W., & Kuehr, H. 1989, A&AS, 80, 103
Stickel, M., Fried, J. W., & Kuehr, H. 1993a, A&AS, 98, 393
Stickel, M., & Kuehr, H. 1993, A&AS, 100, 395
Stickel, M., Kuehr, H., & Fried, J. W. 1993b, A&AS, 97, 483
Stickel, M., & Kuhr, H. 1993, A&AS, 101, 521
Stickel, M., Padovani, P., Urry, C. M., Fried, J. W., & Kuehr, H. 1991, ApJ, 374, 431
Tadhunter, C. N., Morganti, R., di Serego Alighieri, S., Fosbury, R. A. E., & Danziger, I. J. 1993, MNRAS, 263, 999
Thorne, K. S. 1974, ApJ, 191, 507
Urry, C. M., & Padovani, P. 1995, PASP, 107, 803
Vestergaard, M., & Osmer, P. S. 2009, ApJ, 699, 800
Vestergaard, M., & Peterson, B. M. 2006, ApJ, 641, 689
Wampler, E. J., Gaskell, C. M., Burke, W. L., & Baldwin, J. A. 1984, ApJ, 276, 403
Wandel, A., Peterson, B. M., & Malkan, M. A. 1999, ApJ, 526, 579
Wang, J.-M., Luo, B., & Ho, L. C. 2004, ApJL, 615, L9
Warren, S. J., & Møller, P. 1996, A&A, 311, 25
Wilkes, B. J. 1986, MNRAS, 218, 331
Willott, C. J., Rawlings, S., Blundell, K. M., & Lacy, M. 1999, MNRAS, 309, 1017
Wills, B. J., Wills, D., Breger, M., Antonucci, R. R. J., & Barvainis, R. 1992, ApJ, 398, 454
Wills, B. J., Thompson, K. L., Han, M., et al. 1995, ApJ, 447, 139
Wilms, J., Reynolds, C. S., Begelman, M. C., et al. 2001, MNRAS, 328, L27
Woo, J.-H., & Urry, C. M. 2002, ApJ, 579, 530
Woo, J.-H., Urry, C. M., van der Marel, R. P., Lira, P., & Maza, J. 2005, ApJ, 631, 762
Wu, X.-B., Liu, F. K., & Zhang, T. Z. 2002, A&A, 389, 742
Xie, G. Z., Liu, F. K., Liu, B. F., et al. 1991, A&A, 249, 65
Xie, G. Z., Zhou, S. B., & Liang, E. W. 2004, AJ, 127, 53
Xiong, D. R., & Zhang, X. 2014, MNRAS, 441, 3375
Zamaninasab, M., Clausen-Brown, E., Savolainen, T., & Tchekhovskoy, A. 2014, Natur, 510, 126
Zhang, L., Chen, S., Xiao, H., Cai, J., & Fan, J. 2020, ApJ, 897, 10
Zhou, M., & Cao, X.-W. 2009, RAA, 9, 293